# STUDY OF TRANSITION ON A FLARED CONE WITH FORCED DIRECT NUMERICAL SIMULATION

by

**Andrew James Shuck**

**A Thesis**

*Submitted to the Faculty of Purdue University*

*In Partial Fulfillment of the Requirements for the degree of*

**Master of Science in Aeronautics and Astronautics**

School of Aeronautics and Astronautics

West Lafayette, Indiana

August 2021

# THE PURDUE UNIVERSITY GRADUATE SCHOOL
# STATEMENT OF COMMITTEE APPROVAL

**Dr. Jonathan Poggie, Chair**

School of Aeronautics and Astronautics

**Dr. Gregory Blaisdell, Co-Chair**

School of Aeronautics and Astronautics

**Dr. Joseph Jewell**

School of Aeronautics and Astronautics

**Approved by:**

Dr. Gregory Blaisdell

## ACKNOWLEDGMENTS

I would like to thank my friends and family for supporting me throughout my academic career and especially during my thesis work. They have been very understanding and helpful when I have been working. Additionally, I would like to give great thanks to my advisor, Dr. Jonathan Poggie, for offering me this research position and guiding me as I progressed through my research. His advice and insights have been very helpful and greatly improved my understanding. I want to thank Dr. Gregory Blaisdell for his contributions and insights towards my work. They have been invaluable. Finally, I would like to offer my thanks to Dr. Joseph Jewell for accepting the invitation to my committee and the help he provided.

The presented work is supported by the Air Force Research Lab under contract FA8650-20-2-2405 with program manager Christopher Murawski. This thesis was cleared for public release on August 17, 2021 with case number AFRL-2021-2697. Computational resources are provided by the Air Force Research Lab DoD Supercomputing Resource Center, the Engineer Research and Development Center DoD Supercomputing Resource Center, and the Navy DoD Supercomputing Resource Center.

# TABLE OF CONTENTS

# LIST OF TABLES

# LIST OF FIGURES

# LIST OF SYMBOLS

| | |
|---|---|
| $A$ | Random forcing amplitude |
| $a$ | Speed of sound |
| $a_0, a_1, a_t$ | Keyes viscosity constants |
| $a_\mathrm{i}$ | Random forcing amplitude constant |
| $C$ | Partial flared cone circumference |
| $\mathbf{f}$ | Body force |
| $f$ | Frequency used in second-mode estimation |
| $k$ | Wavenumber |
| $\mathbf{n}$ | Unit normal vector |
| $r$ | Radius of flared cone |
| $T$ | Temperature |
| $t$ | Time |
| $V$ | Local flow speed |
| $v_\mathrm{e}$ | Boundary layer edge velocity |
| $w$ | Frequency used in linear stability theory |
| $\mathbf{x}$ | Position vector |
| $\alpha$ | Wavenumber in x direction |
| $\beta$ | Wavenumber in z direction |
| $\Delta_\mathrm{e}$ | Cell edge length |
| $\delta$ | Boundary layer thickness |
| $\mu$ | Viscosity |
| $\mu_0$ | Sutherland viscosity constant |
| $\mathbf{\Phi}$ | Scalarg phase function |
| $\phi$ | Phase shift |
| $\Psi$ | Eigenfunction for disturbance variable |
| $\mathbf{\Psi}$ | Vector wave function |
| $\Omega_k$ | Resolved azimuthal angle |
| $\omega_\mathrm{i}$ | Angular frequency |

# ABBREVIATIONS

| | |
|---|---|
| AFOSR | Air Force Office of Scientific Research |
| BAM6QT | Boeing/AFOSR Mach 6 Quiet Tunnel |
| CFD | Computational Fluid Dynamics |
| DNS | Direct Numerical Simulation |
| LASTRAC | Langley Stability and Transition Analysis Code |
| LST | Linear Stability Theory |

# ABSTRACT

High speed boundary layers are an important aspect of vehicle design. It is crucial to know whether the boundary layer is laminar, turbulent, or transitional. The heat transfer rate increases dramatically from laminar to turbulent flow, so it must be considered when designing a high speed vehicle. This thesis studied a flared cone geometry with forced direct numerical simulation. This geometry has experimental data collected from a Mach 6 quiet tunnel and previous computational data. A two stage computational procedure is carried out in order to efficiently model the boundary layer. The first stage involved finding a full cone solution and creating an inlet profile. This inlet profile is imposed on the inlet of a 10-degree sector of the flared cone. This is done to achieve the desired resolution while maintaining reasonable computational costs for the DNS. With this setup, the second stage continues with a high-order basic state computation using the inlet profile. After the higher order basic state is computed, random forcing is applied using traveling plane waves to promote transition and the results are analyzed. Linear stability and frequency analysis is conducted and the unstable frequencies match with expected results. Transition is achieved using the forcing and qualitatively matches previous experimental and computational data for the flared cone. Just as in the experiment and previous computations, regions of primary and secondary streaks are found and have similar heat transfer magnitudes. However, the location of these streaks is different and is likely due to the setup of the computation.

# 1. INTRODUCTION

High speed flows are an area of interest as people are trying to understand the underlying mechanisms to create vehicles that move faster through the atmosphere. One key factor in this is the boundary layer and understanding how it affects heat transfer rate in this regime. The boundary layer is the thin layer of viscous-dominated flow near the surface where the freestream flow interacts with the surface. It can be laminar, turbulent, or transitional. The laminar boundary layer has a lower heat transfer rate and a turbulent boundary layer has a higher heat transfer rate. For high speed vehicles, it is important to be able to predict when laminar to turbulent transition occurs as the heat transfer rate increases dramatically. However, the transition process is highly nonlinear and depends on a multitude of factors. This makes it very important to be able to replicate the atmospheric perturbations in wind tunnels or computational fluid dynamics. If not, it is difficult to observe the relevant physics in this regime and make correct predictions for vehicle design. Quiet tunnels are created to produce very low freestream noise levels. The Boeing/AFOSR Mach 6 Quiet tunnel at Purdue University is designed in a way to maintain laminar sidewall boundary layers and approach atmospheric noise levels. According to measurements taken by Steen, the freestream pressure fluctuations are lower than 0.02% of the mean whereas noisy flow in the same tunnel is between 1.5 and 4.5% [1]. At quiet levels, the underlying transition mechanisms and features are observable. One example is the second mode instability, which is the main cause of transition for high speed flow. To capture the second mode instability and nonlinear effects in CFD, one must use carry out direct numerical simulations of the Navier-Stokes equations. This form of CFD is the most resource intensive as it directly computes all relevant scales of the flow. It is usually carried out on supercomputers, which involve thousands of interconnected nodes, each with dozens of compute cores. One way to get an estimation of the stability of the flow, without using DNS, is to use Linear Stability Theory. LST can predict the frequency that will be amplified and be the most likely cause of transition. However, as its name suggests, it cannot predict the nonlinear regime which includes the period where the instabilities breakdown to turbulence. This thesis will investigate a flared cone geometry that has been investigated experimentally in the BAM6QT by Chynoweth [2] and numerically through DNS computations carried out by Hader [3]. A more natural forcing technique is used to promote transition. It involves using traveling plane waves to more accurately model freestream perturbations. Additionally, the magnitude of the forcing can be aligned with wind tunnel data. Multiple forcing profiles related to the BAM6QT will be applied to obtain transition and validate this method of forcing.

This chapter presents information regarding the history and process of Laminar Turbulent Transition, the theory and mechanics behind Linear Stability Theory, previous studies carried out on the flared cone, and the scope of research conducted for this thesis. At the end, all of the chapters in this thesis are briefly explained.

## 1.1 Laminar-Turbulent Transition

The process of transitioning from laminar to turbulent flow consists of three main scenarios, natural transition, bypass transition, or separated-flow transition [4]. Natural transition is the scenario of interest because it follows a process where small disturbances enter the boundary layer through receptivity, and develop into 3D structures which can breakdown into fully turbulent flow. More specifically, the beginning of transition starts with the generation of Tollmien-Schlichting waves, which appear as 2D waves. These waves can then develop secondary instabilities and continue into the nonlinear regime and form complex vortices. If the instabilities continue to grow, these vortices will continue to breakdown and proceed to turbulence [5]. The other two cases, bypass and separated-flow transition, can bypass parts of this natural process and go directly to vortex breakdown and turbulence formation. Bypass transition occurs when there is strong forcing, such as rough walls or very noisy freestream. These strong forces can cause spots of turbulence to form directly in the boundary layer. The analysis of the production, growth, and convection of these turbulent spots are essential to bypass transition analysis [6]. Separated-flow transition happens when a boundary layer separates from the surface and reattaches as turbulent. The region where the laminar flow separates and reattaches as turbulent forms a “bubble” which can cause loss in efficiency [6]. Interestingly, if the flow is low noise, then part of the natural transition process can possibly be detected in the bubble [7]. For the flared cone, natural transition is the scenario that is occurring as experiments are conducted in a quiet tunnel, the surface is smooth, and the flow does not separate.

The high speed laminar-turbulent transition process on the flared cone follows the natural transition path. Although the BAM6QT freestream is quiet relative to conventional tunnels, a noise field does exist, and processed through receptivity. This noise forms the initial disturbance amplitude in the boundary layer. The instabilities in this low noise system can grow by first mode, second mode, crossflow instability, or Görtler vortices [8]. Each of these involve the eigenmode growth of unstable normal modes until nonlinear breakdown. The first mode instability involves the generation and growth of the Tollmien-Schlichting waves, as described above. The crossflow instability involves a 3-D velocity profile of a boundary layer caused by the imbalance between centripetal acceleration and pressure gradient on a swept surface. At the wall and far from the wall, there is no crossflow velocity, so an inflection point exists and is the source of the crossflow instability [9]. The Görtler instability occurs on concave surfaces and results in counter-rotating streamwise vortices. These vortices form from the centrifugal force as the flow travels along the curved surface [10]. Finally, the second mode instability is a type of acoustic wave trapped in the boundary layer. This boundary layer acts as a waveguide with the acoustic waves being contained by the wall and the sonic line [8], [11]. This type of acoustic wave occurs when “there is an embedded region of supersonic flow relative to the phase speed”[12]. Additionally, at freestream conditions higher than Mach 4, the second mode is predicted to be the most unstable mode [12]. Experiments conducted by Potter and Whitfield[13], were able to observe the signs of second-mode transition on a cone. Long regions of what they termed “rope waves” were observed before transition occurred [13].

During the process of laminar-turbulent transition, many nonlinear interactions occur which are hard to describe. One vector where these interactions occur is through the formation and breakdown of hairpin vortices. Experiments by Klebanoff et al. investigated three dimensional boundary layer instabilities and the effect hairpin vortices have on the transition process [14]. He found there were spanwise periodic patterns appearing in the boundary layer. Computations conducted by Bake et al. used DNS to match with experimental results and found $\Lambda$ vortices forming at various spanwise locations and hairpin vortices evolving from them. These hairpins then have many nonlinear interactions with the freestream and eventually breakdown [15]. This type of breakdown is considered a Klebanoff (K-type) secondary instability.

### 1.2 Linear Stability Theory

Now that the general transition process has been described, it is important to consider the likelihood of transition for a given geometry and flow condition. Identifying and predicting this starts with determining the unstable modes for a given flow. For second-mode waves, and estimation can be given by the equation

$$f = \frac{v_{\mathrm{e}}}{2\delta}, \tag{1.1}$$

where $v_{\mathrm{e}}$ is the edge velocity, $\delta$ is the boundary layer height, and $f$ is the unstable second-mode frequency. For example, if the edge velocity was 646 m/s and the boundary layer was around 1 mm, then the frequency for the second mode waves are around 320 kHz. As described in the previous section, the second-mode wave is an acoustic wave trapped within the boundary layer. With the boundary layer acting as a waveguide, the acoustic wave must fit within it. For more thorough analysis, Linear stability theory, LST, is used. It can do this by adding small, arbitrary disturbances to the velocity and pressure to the Navier-Stokes equations and linearizing by assuming products of the disturbances are negligible [12], [16]. The governing equations can be written in a separable form and have normal mode solutions as seen the equation,

$$\Psi = \Psi'(y)\mathrm{e}^{i(\alpha x+\beta z-wt)}, \tag{1.2}$$

where $\Psi'$ is the velocity, pressure, or temperature eigenfunction, $\alpha$ and $\beta$ are wavenumber components, and $w$ is the frequency. The type of wave can give insight into the stability of the flow. If $\alpha$, $\beta$, and $w$ have a non-zero imaginary part, then the wave will change in amplitude, otherwise if they are all real, then it will be neutrally stable. In order to solve these equations, the boundary conditions must be chosen. For a boundary layer, one condition is that the disturbances approach zero far from the wall, and the other one is the no-slip condition [12]. With this, the equations can be solved. A common way to represent the amplification of these disturbances is to use the $e^N$ method. It compares the amplitude of the disturbance of an initial point to the amplitude of points at locations downstream of the initial point. This allows the tracking of growth and decay as it moves along the surface. For low speed flow over wings, plates, and other geometries, an N-factor of 8 to 11 seem to be the value where transition occurs most often [17], [18].

### 1.3 Studies on High-Speed Boundary Layer Transition

The flared cone was used in experiments at the BAM6QT at Purdue University. The BAM6QT is a Ludwieg tube and its nozzle is designed to produce exceptionally quiet flow. A Ludwieg tube works by having a pressure tank at one side and a vacuum tank at the other. Once a certain pressure differential is achieved, a burst disc breaks and the tunnel run starts. The total test duration is 5 s or less and has quasi-steady flow intervals of 0.2 s as expansion waves reflect up and down the tube. With this short duration, an isothermal surface boundary condition can be used in computations. Following his experiments in this wind tunnel, Chynoweth successfully observed transition on the flared cone and recorded a set of primary and secondary streaks using temperature sensitive paint. Temperature sensitive paint is used to obtain approximate heat transfer rates and can be considered time-averaged. His results from Run 1611 can be seen in Figure 1.1. From this, he is able to generate streamwise and spanwise plots of heat transfer available in Figure 1.2 and 1.3. Chynoweth conducted multiple experiments at different Reynolds number and found that the unstable mode increases frequency as Reynolds increases. At the conditions for Run 1611, the second-mode frequency is around 340 kHz.

Along with experimental results, DNS was conducted by Hader using various forcing methods. These included a controlled disturbance input and a natural disturbance input which are both input at a slot on the surface, the inlet boundary, or a combination of the two [3]. The controlled forcing and random forcing cases will be referred to in this thesis as Case HC and Case HR, respectively. To control the flow and cause it to transition, the most unstable frequency, around 300 kHz, is input for as the input for Case HC. Using

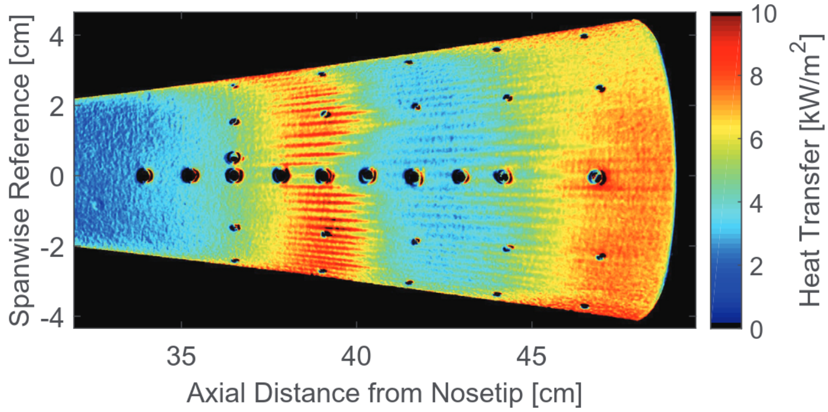


**Figure 1.1.** Experimental transition on the flared cone with heat transfer contours. Used with permission of the author [2].

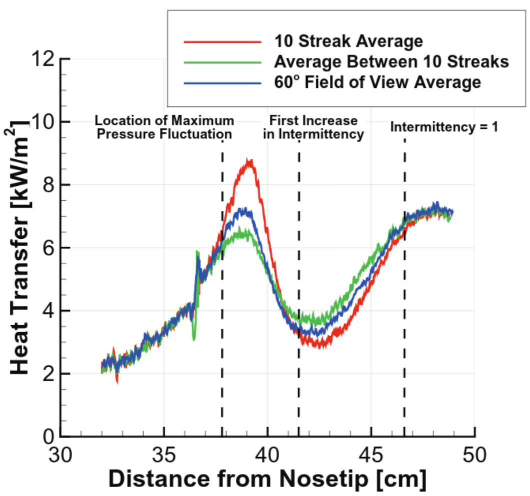


**Figure 1.2.** Streamwise heat transfer profile averaged across various methods [2].

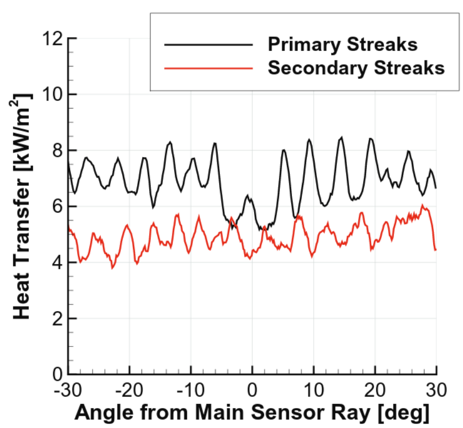


**Figure 1.3.** Spanwise heat transfer extracted at the primary and secondary streak locations [2].

the controlled forcing method, Case HC successfully captures the two regions of streaks at nearly the same location as the experiment. Case HR used random pressure fluctuations at the inlet of the domain to simulate acoustic noise. Using this more natural method, Hader was able to see transition in a similar manner, although slightly different. The results of these two methods can be seen in Figure 1.4. Additionally, the structures of the streaks were investigated by creating iso-surfaces of Q-criteria in Case HC seen in Figure 1.5. Hader found evidence for Klebanoff type breakdown with $\Lambda$ vortices which evolve into hairpin vortices as nonlinear effects start to occur.

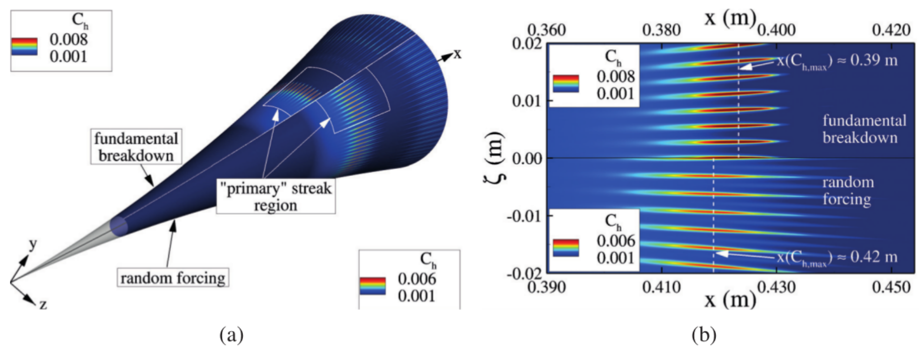


**Figure 1.4.** (a) Time-averaged Stanton number. Left is controlled forcing (Case HC), right is random forcing (Case HR). (b) Closer view of Stanton number. Top is controlled forcing, bottom is random forcing. Used with permission of the author [3].

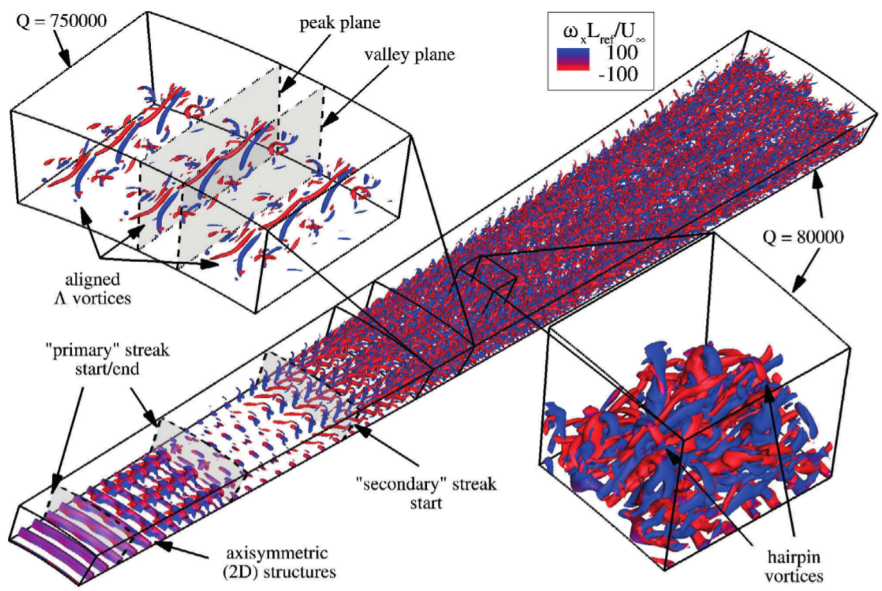


**Figure 1.5.** Iso-surfaces detailing the structure of the flow during transition of the controlled forcing case (Case HC). Used with permission by author [3].

### 1.4 Scope of Research

This thesis aims to reproduce the transition process observed experimentally by Chynoweth [2] and computationally by Hader [3], [19] by introducing random disturbances into the flow. The disturbances are introduced into the freestream as a body force using randomly characterized traveling plane waves. These waves model freestream noise that exists in a wind tunnel or the atmosphere more naturally compared to Hader's work. Additionally, wind tunnel noise profiles are applied to the forcing amplitude to more closely align with wind tunnel conditions. This will allow a more natural and accurate transition process compared to uniform forcing. Using this, the DNS will try to obtain results of heat transfer rate that matches the pattern of primary and secondary streaks. Success with this method will validate this type of random forcing along with the usage of wind tunnel noise profiles.

Chapter 2 covers the freestream conditions in detail and what tools and processes were chosen to compute the flared cone. It discusses the procedure and explains the mesh generation along with Kestrel and Wabash, the CFD solvers that are used. Kestrel is an unstructured finite volume code created by the DoD and is optimized for various air vehicles. It has many options which are explained in this chapter. Wabash is a very capable structured solver which can introduce the random forcing into the freestream. This, and other capabilities in Wabash, are discussed here. In order to help validate the CFD results, a linear stability theory code, LASTRAC, is used and is also explained in Chapter 2. Finally the machines where these codes are executed are described along with some details of carrying out computations on large clusters.

Chapter 3 discusses the results of Kestrel, Wabash, and LASTRAC. It covers the comparison of Kestrel and low-order Wabash calculations and the results of a high resolution Kestrel run that creates the inflow condition for DNS. The DNS involves multiple cases of different random forcing, these results are each briefly discussed and then compared in detail with each other and with Hader's and Chynoweth's results.

Finally, Chapter 4 discusses the conclusions gathered from these results, what could have been done better, and suggests ideas to expand upon this research.

# 2. METHODOLOGY

This chapter describes the geometry, flow conditions, mesh, and the tools used to compute and analyze the flared cone. There are three different solvers used, each with its own purpose. Kestrel is a lower order accuracy, unstructured-grid CFD solver that can generate solutions quickly. Wabash is the high-order solver which is used to carry out the large computations. It can also be switched to a lower order mode and is compared to Kestrel. LASTRAC is the LST tool used to analyze the basic state of the flow and predict which frequencies are unstable. There is a section describing noise profiles from the BAM6QT and how they are implemented in Wabash. Finally, the machines these computations are carried out on are described along with a few details about computing on large clusters.

## 2.1 Geometry and Flow Conditions

The flared cone geometry is given by Chynoweth [2]. There are detailed drawings which describe the shape and geometry of the cone. The surface of the cone is created from a 3 meter radius circle and with a nosetip of 0.0001 m. This simple geometry allows the use of algebraic expressions for grid generation. The radius for the surface of the cone can be described with the equation,

$$r = \sqrt{9 + (x + 0.08)^2} - 3.001, \tag{2.1}$$

where $x$ is the axial distance and $r$ is the radius. This curve can be seen in Figure 2.1, with a curve revolved around the $x$-axis in Figure 2.2. The flow conditions used in this thesis are based on BAM6QT Run 1611 by Chynoweth and are detailed in Table 2.1. The model has a length of 0.51 m and the computational domain was extended to 0.6 m to allow extra space for the boundary layer to transition. The design of the BAM6QT allows a total run time of 5 s, so an isothermal wall condition is used. Furthermore, the gas is considered a perfect gas as the freestream temperatures are low. With these low temperatures, the viscosity model may become an issue so it is necessary to investigate multiple options. The Sutherland's

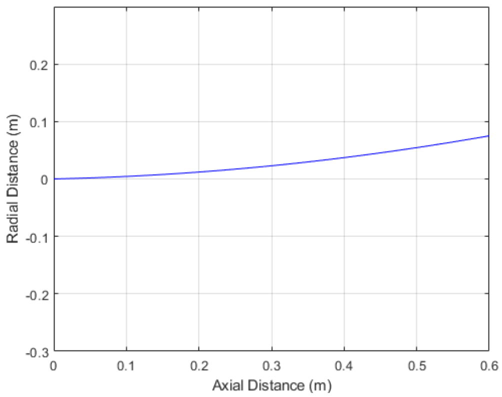


**Figure 2.1.** Flared Cone Surface Equation

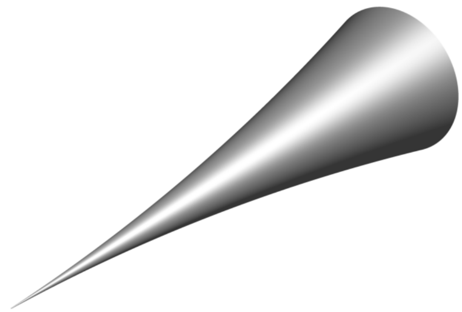

**Figure 2.2.** Flared Cone Geometry

**Table 2.1**. Freestream Conditions

| Parameter | Value |
|---|---|
| Mach | 6 |
| Freestream Velocity | 864 m/s |
| Freestream Pressure | 684 Pa |
| Freestream Temperature | 51.46 K |
| Unit Reynolds Number | 12E6/m |
| Isothermal Surface Temp | 300 K |

formula has an error of <2% for temperatures in the range of 170-1900 K [4], [20], and it is defined for air by the equation,

$$\mu = \mu_0 \left(\frac{T}{T_0}\right)^{\frac{3}{2}} \left(\frac{T_0 + 110.4}{T + 110.4}\right). \tag{2.2}$$

Reference temperature and viscosity are given by $T_0$ and $\mu_0$, respectively, and the temperature of interest is given by $T$. This flow is outside the range for the Sutherland's equation, at 51 K. A lower temperature model, the Keyes model, is investigated to be a potential replacement. It is defined with the equation,

$$\mu = \left(\frac{a_0\sqrt{T}}{1 + a_1\tau/10^{a_t\tau}}\right) \cdot 1 \times 10^{-6}, \tag{2.3}$$

where $a_1$, $a_t$, and $a_0$ are constants and $\tau$ is equal to $T^{-1}$. Additionally, it is valid for temperatures in the range of 90-1845K [21]. The freestream temperature of 50 K lies below even this extended range. The two models are compared in Figure 2.3, 2.4 and it details differences of around a 10% at 50 K. Within the intended ranges, the percent difference is below 2%. With both being slightly outside of their intended range at the freestream temperature, determining which one is better would require more thorough study. In the end, Sutherland's equation is chosen.

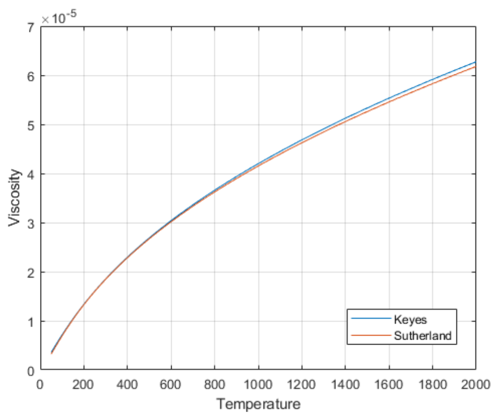


**Figure 2.3.** Viscosity model comparison.

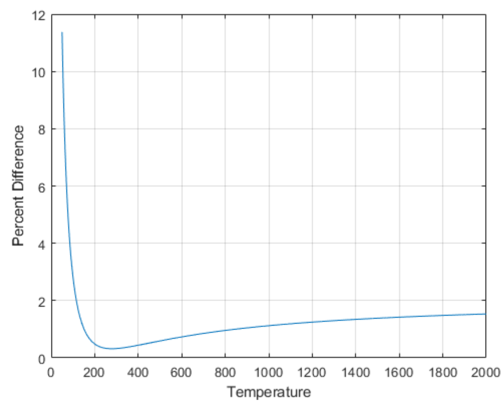


**Figure 2.4.** Viscosity model % difference w.r.t. Sutherland's equation.

## 2.2 Computational Procedure

There is a large difference in scale between the nosetip and the length of the cone. This can cause some issues with going directly to a high-order Wabash calculation on the whole cone. As the distance from the nosetip decreases, the azimuthal cell edge length decreases significantly. For Wabash, only global timestepping is used, so the maximum stable time step is based on the smallest cell. With a small enough cell length, the computation could potentially take months to compute. In order to overcome this obstacle, local time stepping in Kestrel is used to generate an initial lower-order basic state solution of the full 3D geometry. With this, a profile normal to the surface can be extracted and used as an input to the high-order Wabash calculation. The extract is applied to and held constant at the entire inlet plane of the high-order Wabash calculation. A comparison between the Kestrel and Wabash on a common grid will provide confidence in this process and in this thesis the DNS will refer to the high-order Wabash calculation.

With the nosetip removed, the DNS can model the rest of the cone with much higher resolution. Even with this method, only a few degrees of the cone in the circumferential direction can be used. This is because the cost of DNS is much higher than a low-order basic state calculation; a DNS with the whole 360° cone would consist of tens of billions of cells and require far too many resources. In order to calculate the high-order basic state from the inlet condition, a two stage process is carried out in Wabash to increase the stability of the calculation. The computation starts off lower order and is switched to higher order to finish the basic state. Once the basic state solution for DNS is developed, noise can be introduced to model the atmospheric perturbations or specific wind tunnel profiles. The noise will be adjusted until it reaches a sufficient strength and transition is achieved. Finally, LASTRAC is carried out on both the Kestrel and the Wabash basic states. It requires a 2D slice of each and can be easily extracted and computed from the basic state solutions.

### 2.3 Mesh

In this thesis, the indices i, j, and k correspond to the axial, wall normal, and azimuthal mesh directions, respectively. The comparison of Kestrel and Wabash involve a common mesh where the nosetip is numerically sharp. After this is completed, a modeled nosetip mesh is created and used in Kestrel to create a low-order basic state solution to extract the inlet condition. Both the modeled nosetip mesh and the numerically sharp nosetip mesh are similar and created with the following process. A 2D axisymmetric mesh is generated using Equation 2.1, and each nosetip type is added to the front. From this, the grid is revolved and refined in Pointwise. Part of this refinement for the modeled nosetip mesh is adding an O-grid on the nosetip to bypass a singularity that would result from rotating a 2D grid. These meshes can be seen in Figure 2.5 along with magnified nosetips in Figure 2.6 and Figure 2.7. A sponge layer is added at the rear of the cone to dissipate any reflections and numerical noise at the boundary and the overall mesh dimensions are available in Table 2.2.

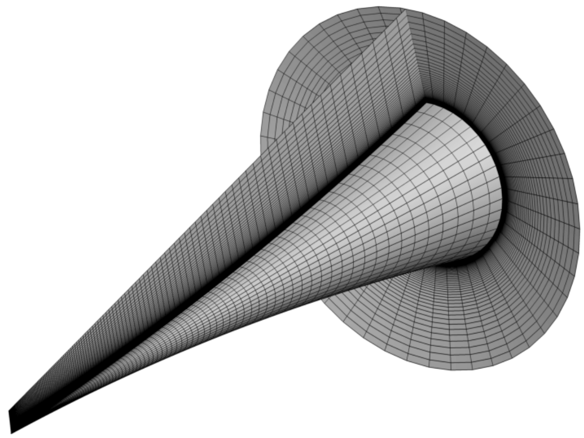

**Figure 2.5.** Kestrel Grid Overview

**Table 2.2**. Grid details for the code comparison and low-order basic state solution. Only Kestrel is used for the low-order basic state solution.

| Parameter | Low-Order Basic State | Code Comparison |
|---|---|---|
| Nosetip Type | Modelled | Numerically Sharp |
| Total Cells | 260E6 | 65E6 |
| Nosetip Cells(unstructured) | 9E6 | N/A |
| Body Cells(structured) | 251E6 | 65E6 |
| Initial Wall Spacing | $5 \times 10^{-6}$ | $10 \times 10^{-6}$ |
| Axial Resolution (i) | 844 | 600 |
| Wall Normal Resolution (j) | 600 | 600 |
| Azimuthal Resolution (k) | 500 | 181 |
| Degrees/Cell | $0.72^{o}$ | $2^{o}$ |

As mentioned in Section 2.2, the nosetip for the DNS (Wabash) will have to be cut off to maintain a reasonable time step. The resolution is guided by the approach that Hader [19] used for his work on this geometry. The azimuthal resolution is important as there are streaks found by Chynoweth and Hader [2], [19]. In order to create the cone, Equation 2.1 is rearranged to determine how much of the cone would need to be cut off for a certain azimuthal resolution and angle. With the azimuthal angle and resolution, the radius is known and the $x$ cut off value can be found. This is done by determining a partial circumference using the

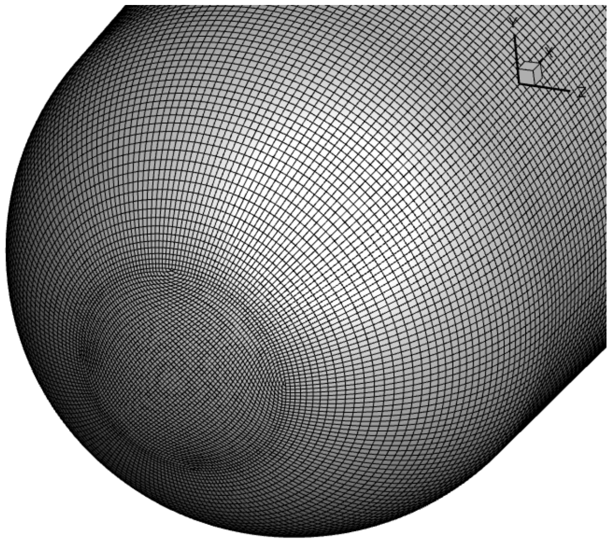

**Figure 2.6.** Kestrel Nosetip Grid

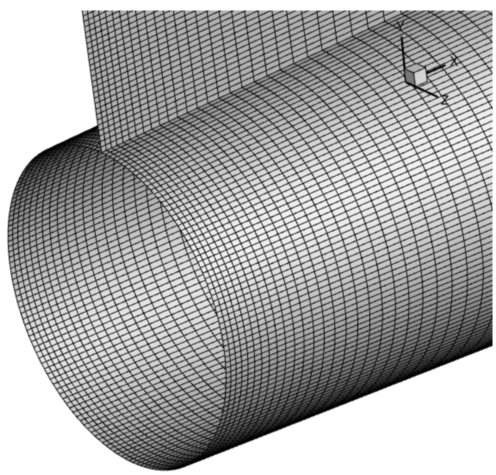

**Figure 2.7.** Sharp Nosetip Grid

minimum edge length and the azimuthal resolution. Then, the partial circumference and azimuthal angle can find the radius and $x$ value. This process can be seen in the equations

$$\begin{aligned}
\Delta_{\mathrm{e}} &= 1 \times 10^{-5} m,\ \Omega_k = 10^{\mathrm{o}} = \pi/18, \\
k_{\max} &= 400 \text{ cells}, \\
C &= k_{\max} * \Delta_{\mathrm{e}}, \\
r &= C/\Omega_k, \\
x_{\mathrm{cut}} &= \sqrt{(r+3.001)^2 - 9} - 0.08,
\end{aligned} \tag{2.4}$$

where $\Delta_e$ is the minimum edge length, $C$ is the partial circumference, $k_{max}$ is the max resolution in the $k$ direction, and $\Omega_k$ is the azimuthal angle being resolved measured in radians. The target azimuthal resolution is around 0.035 degrees/cell and the minimum edge length to obtain a reasonable time step is around $1 \times 10^{-5}$. In this case, the values for azimuthal resolution and angle are 400 cells and 10°, respectively, and results in the DNS grid starting at 0.3m from the nosetip. With so much of the cone cut off, it is extended and resolved until 0.6m; 0.09m longer than experiment. This allows more time for the unstable modes to grow and develop if it does not transition before the end of the model. The grid is generated algebraically and the details are available in Table 2.3. A sponge layer that grows with a stretching ratio of 1.2 is used at the rear of the cone to damp out any numerical noise originating at the boundary. The resulting computational domain can be seen in Figure 2.8. Additionally, extra space above the shock was included in the grid to allow generation of noise in the freestream.

**Table 2.3**. Wabash Grid Details

| **Parameter** | **Value** |
|---|---|
| Total cells | 1282E6 |
| Angle modeled | 10° |
| Cut off location | 0.30 m |
| Initial wall spacing | $1 \times 10^{-5}$ |
| Axial Resolution (i) | 4025 |
| Wall normal resolution (j) | 801 |
| Azimuthal resolution (k) | 400 |
| Degrees/Cell | 0.025° |
| Boundary layer cells | 100 |
| Time step | $1.3 \times 10^{-8}$ s |
| Sampling frequency | 77 MHz |

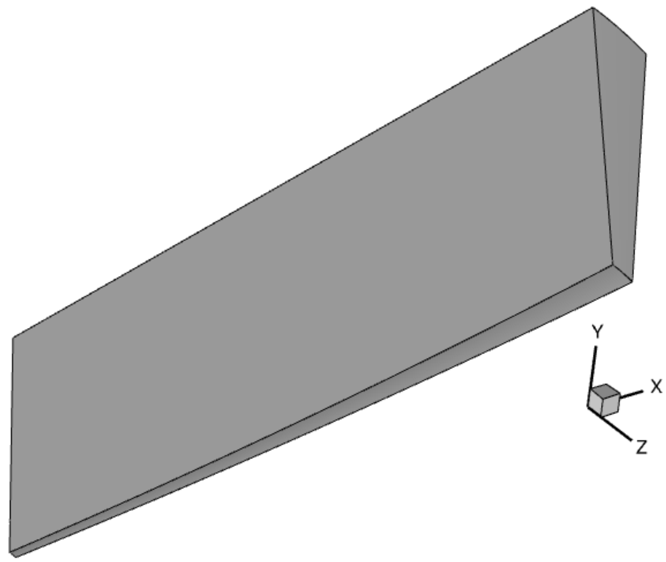


**Figure 2.8.** Wabash Computational Domain.

## 2.4 Kestrel

Kestrel is a CFD solver which is optimized to generate efficient and accurate solutions for various air vehicles. It is developed by the DoD CREATE$^{TM}$ team and is used to improve "DoD acquisition program timeline, cost, and performance"[22]. It regularly receives updates improving its capabilities. Some recent or planned developments involve implementing an unstructured adaptive mesh refinement technique, thermochemical capabilities, and better user interface and workflow. More details about the development and usage can be found in [23]–[25]. The main component used in this thesis, KCFD, is an unstructured, finite volume solver that can use second-order accurate space and time. It has the ability to use Euler, laminar, or turbulent flow with the Spalart-Allmaras and Menter turbulence models or the Menter one-equation transition model. KCFD can do global and local time stepping depending if time-accurate solutions are desired. Additionally, there are a multitude of available boundary conditions that are useful for many different types of CFD cases. For this thesis, the options chosen for this case are summarized in Table 2.4. The boundary

**Table 2.4**. Kestrel Configuration

| | |
|---|---|
| Equation set | Navier-Stokes |
| Turbulence model | None |
| Spatial accuracy | Second-order |
| Temporal accuracy | First-order |
| Time stepping | Local |

conditions consisted of a no-slip condition with an isothermal wall at 300 K. The inlet is a farfield condition and the sponge layer allows the outlet to also be a farfield. The boundary conditions can be seen in Figure 2.9. The flow is calculated as laminar using local time stepping with an initial Courant-Friedrichs-Lewy (CFL) number of 100. As the solution progresses, the CFL increases up to a value of 1000. The spatial accuracy is the highest available at second-order accuracy. The temporal accuracy is chosen as first-order to more quickly progress to a steady state solution. The inviscid flux scheme is HLLE++ and the viscous flux is LDD+.

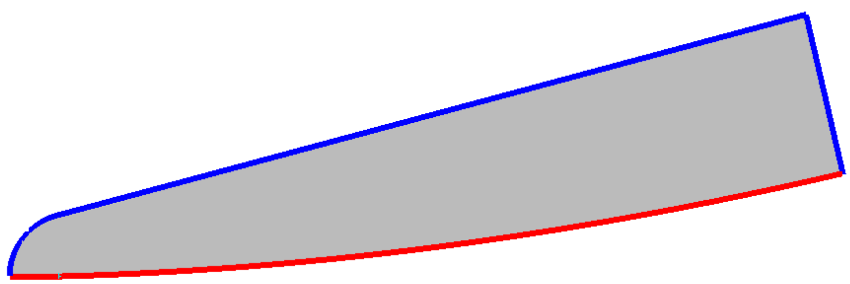

**Figure 2.9.** Kestrel Boundary Conditions: red is wall, blue is farfield.

## 2.5 Wabash

### 2.5.1 Capabilities

Wabash, formerly known as HOPS (Higher Order Plasma Solver), is a high-ordered, structured, and overset code being developed by J. Poggie [26]–[29]. It contains various numerical schemes for spatial and temporal discretization. This allows one to improve stability

**Table 2.5**. Wabash Configurations

| | **Low-Order** | **High-Order** |
|---|---|---|
| Spatial Scheme | explicit second-order differencing | implicit sixth-order differencing |
| Temporal Scheme | implicit first-order | explicit fourth-order Runge-Kutta |
| Time Step | Adaptive, based on smallest cell CFL | Fixed at $1.1 \times 10^{-5}$ |
| Upwinding | Roe scheme | Compact scheme & Roe scheme near shocks |
| Shock Detector | Off | On |
| High-Order Filtering | Off | On, template begins with eigth-order |

of a solution by starting with a low-order scheme and switching to a high-order scheme. This process is carried out for the DNS basic state. The lower-order computation uses 2nd-order differencing and first-order implicit time stepping to best prepare the solution for more unstable high-order schemes. Once the lower-order calculation is completed, the spatial discretization is switched to implicit sixth-order compact differencing and the temporal discretization is switched to explicit fourth-order Runge-Kutta time stepping. A summary of the options used in this thesis are available in Table 2.5. When the higher-order basic state is completed, random forcing can be injected into the freestream to promote transition. There are various forcing options and they are described in Section 2.5.2. The boundary conditions consist of an inlet profile, an extrapolation outlet, and periodic side walls. Additionally, strong filtering is applied in the sponge layer to damp disturbances originating at the boundary.

### 2.5.2 Freestream Forcing

As mentioned in previously, Wabash has the capability to impose freestream forcing to promote transition. The implementation is similar to that employed by Tufts et al. [30] and Cerminara et al. [31] and involves traveling plane waves composed of randomly generated characteristics. The forcing is created to be fully resolved and continuous across boundaries of domain decomposition. Plane waves are described by the following equations:

$$\begin{aligned} \mathbf{\Psi}(\mathbf{x}, t) &= \mathbf{A} \cos\left[\mathbf{\Phi}(\mathbf{x}, t)\right], \\ \mathbf{\Phi}(\mathbf{x}, t) &= \mathbf{k} \cdot \mathbf{x} - \omega t + \phi, \end{aligned} \tag{2.5}$$

where $\mathbf{\Psi}(\mathbf{x}, t)$ is the vector wave function and $\mathbf{A}$ is the amplitude vector. Furthermore, $\mathbf{\Phi}(\mathbf{x}, t)$ is the scalar phase function with wavenumber vector, angular frequency, and phase shift of $\mathbf{k}$, $\omega$, and $\phi$, respectively. Additionally, the wavenumber vector can be split into wavenumber, $k$, and unit normal vector, $\mathbf{n}$, using $\mathbf{k} = k\mathbf{n}$. In order to accurately create acoustic waves in a moving fluid, the Doppler shift must be accounted for. The following equation adjusts the wavenumber relative to the velocity, $\mathbf{V}$, and the speed of sound, $a$, of the medium.

$$k = w/|a + \mathbf{V} \cdot \mathbf{n}| \tag{2.6}$$

Furthermore, the unit vector, $\mathbf{n}$, can be defined using spherical coordinates as seen in the equations below

$$\begin{aligned} n_1 &= \cos\theta_1, \\ n_2 &= \sin\theta_1 \cos\theta_2, \\ n_3 &= \sin\theta_1 \sin\theta_2, \end{aligned} \tag{2.7}$$

where $\theta_1$ and $\theta_2$ are the polar angle and azimuthal angle, respectively. With this, the acoustic wave can be generated by randomly assigning values to $\theta_1$, $\theta_2$, and $\phi$ for each frequency. The actual forcing is implemented as a body force with the equations:

$$\mathbf{f} = A \sum_{\mathrm{i}} a_{\mathrm{i}} \left[ \frac{\omega_{\mathrm{i}} \mathbf{x} \cdot \mathbf{n}}{|a + V n_1|} - \omega_{\mathrm{i}} t + \phi_{\mathrm{i}} \right] \mathbf{n}, \tag{2.8}$$

where $\mathbf{f}$ is the body force, $A$ is the amplitude, $a_{\mathrm{i}}$ is an amplitude constant, $\omega$ is the angular frequency, $\mathbf{n}$ is the direction of the wave, $a$ is the speed of sound, $V$ is the local flow speed, and $\phi$ is the angular phase [32]. For this thesis, $\mathrm{i} = 201$ and represents evenly spaced modes between the frequencies of 11 kHz and 770 kHz. There is an option to introduce a heat source in a similar manner, but it is not considered in the current work. Additionally, the location is specified by creating a 2D quadrilateral that is revolved around the cone. For example, the beginning and ending $x$ and the height are specified along with an optional slant angle. With the location and type of forcing specified, noise can be implemented and the effect can be observed. Andrews and Poggie [33] have found nonlinear growth resulting from the use of this formulation implemented in Wabash.

Wabash can also specify relative magnitudes for each frequency instead of a uniform distribution. This means the forcing profile can be matched with wind tunnel disturbance spectra. In this case, the BAM6QT has available data collected by Gray [34] for both noisy and quiet flow and are used to create a forcing profile in Wabash. This process of converting the data to a usable form is detailed by Shuck [35] and the resulting equations of best fit are available in Figure 2.10. These equations can then be used in Wabash to generate profiles replicating noise in the BAM6QT. Additionally, Duan et al. conducted a detailed study to characterize the freestream noise in wind tunnels and relate DNS of the wind tunnels to experiment [36]. Duan et al. used DNS to support the experiment and found disturbances quantities that are difficult to obtain otherwise. His work is the first step in a series to compute observed transition in certain wind tunnels using disturbance models.

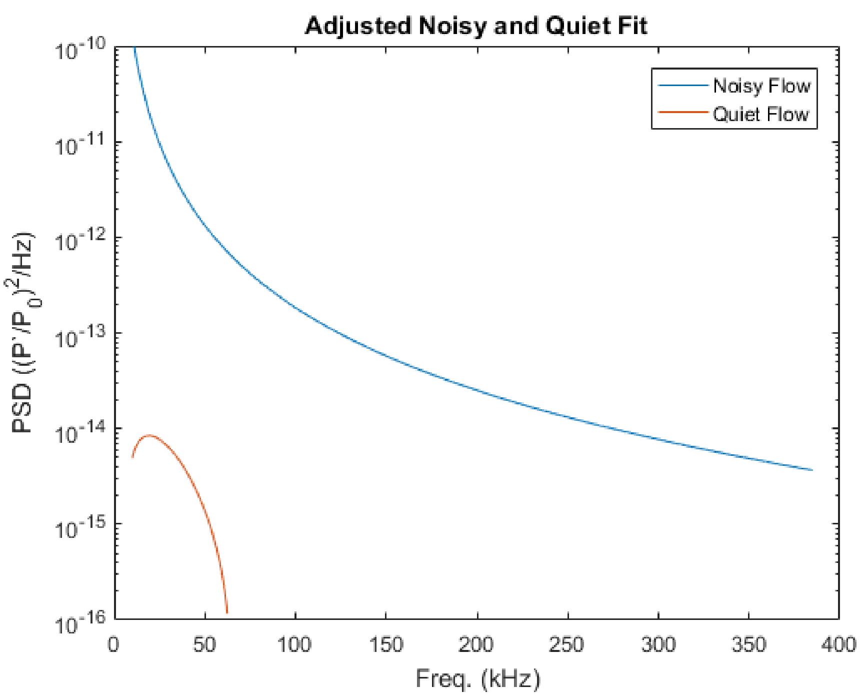


**Figure 2.10.** BAM6QT Noise Profiles

### 2.5.3 Other considerations

Wabash has the capability to be overset which has the potential to solve the nosetip issue. Multiple overset blocks, each decreasing in azimuthal resolution until a numerically sharp nosetip is achieved, can be used to model much more of the cone than a single block can. This involves reducing the azimuthal resolution in stages by a factor of two until it reaches around 20 cells across. This results in a mesh that consists of 6 blocks and can be seen in Figure 2.11. In theory, this is a better option than calculating the nosetip region as a separate solution and imposing it on a DNS solution, however the interpolation accuracy between the grids is currently only second-order. Each time they pass through an overlap, the disturbances will be damped. With this number of blocks, the disturbances will be extremely dampened by the time they reach the final block. With Kestrel being second-order as well, the consideration moves to the computational cost and complexity. The simplest and most cost efficient method is to start with Kestrel and impose an inflow for Wabash. Although the noise cannot grow along the whole length of the cone, the cone has been extended and stronger forcing can be introduced to compensate for that.

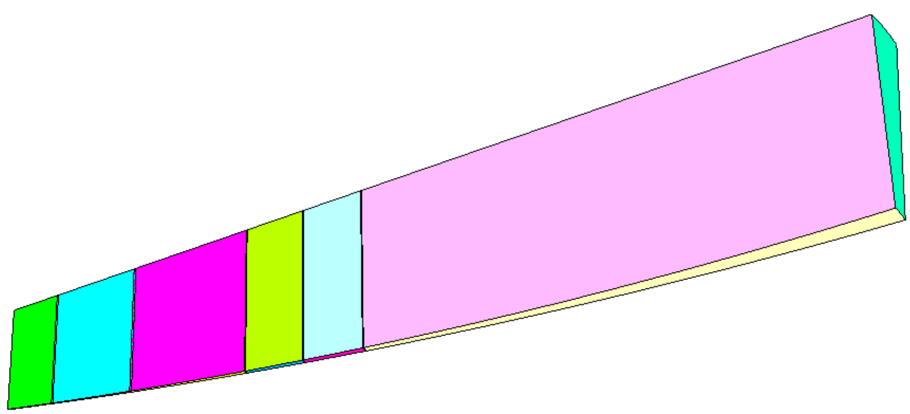

**Figure 2.11.** Overset DNS Domain

## 2.6 LASTRAC

The Langley Stability and Transition Analysis Code, LASTRAC, is a code developed at the NASA Langley Research Center. It was created to “provide an easy-to-use engineering tool for routine use and to incorporate state-of-the-art computational and theoretical findings for integrated transition predictions" [37]. This is accomplished by using LST or PSE to determine the N-factors of various disturbance frequencies. It can be used for 2D, axisymmetric, infinite swept wing boundary layers, and general 3D boundary layers [38]. To use this code, the type of flow being analyzed is specified. In this case, it is a 2D axisymmetric boundary later. Additionally, the type of solution desired is specified and chosen to solve the local eigenvalues. LASTRAC then marches through stations corresponding the the grid points in the i direction and tests frequencies ranging from 10 kHz to 1000 kHz at each station. From this, the N-factors are calculated and unstable frequencies can be identified.

### 2.7 Computational Resources

The majority of the computations carried out for this thesis were completed on two machines, Engineer Research and Development Center's Onyx and Navy DoD Supercomputing Resource Center's Narwhal. Onyx is a Cray CX 40/50 with 4,810 standard compute nodes, each with a dual socket motherboard with two 2.8-GHz Intel Xeon Broadwell 22-core processors and 128 GB of DDR4 memory. Onyx has robust data storage consisting of a work directory of around 13 PB and a home directory of 900 TB. Furthermore, these storage systems are managed by the Lustre file system. This allows them to use parallel I/O which can scale to hunderds of GB per second [39]. This is key for DNS, as the files tend to be very large and there are many write operations taking place when collecting statistics. Narwhal is a HPE Cray EX system recently deployed by the NavyDSRC. It consists of 2176 standard compute nodes, each with two AMD Epyc ROME 7H12 64-core processors and 256 GB of DDR4 memory. Narwhal has similarly sized home and work directories which are also managed by the Lustre file system.

In order to fully utilize resources on a supercomputer, the domain must be split into manageable subdomains. For the compact difference approach employed in this work, Garmann found that an ideal subdomain is around 100x100x100 cells in the i, j, and k directions[40]. To obtain that size of subdomain, the i, j, and k grid dimensions are split into 40, 8, and 4 pieces from a total of 4000, 801, and 400 points, respectively. The number of subdomains in

**Table 2.6**. MPI and OMP Configurations for 1280 ranks

| **Onyx (2x 22 core)** | | | **Narwhal (2x 64 core)** | | |
|---|---|---|---|---|---|
| MPI Processes | OMP Threads | Total Cores | MPI Processes | OMP Threads | Total Cores |
| 4 | 11 | 14,080 (320 nodes) | 128 | 1 | 1,280 (10 nodes) |
| 2 | 22 | 28,160 (640 nodes) | 64 | 2 | 2,560 (20 nodes) |
| 1 | 44 | 56,320 (1280 nodes) | 16 | 8 | 10,240 (80 nodes) |
| 44 | 1 | N/A | 8 | 16 | 20,480 (160 nodes) |
| 22 | 2 | N/A | 2 | 64 | 81,920 (640 nodes) |
| 11 | 4 | N/A | 1 | 128 | 163,840 (1280 nodes) |

this configuration is equal to 1280 and is equal to the number of MPI ranks employed in the calculation. The computer cores are distributed between MPI and OpenMP processes in a specific way to take advantage of node interconnects and shared memory. For example, Onyx has 44 cores per node and if 4 MPI processes per node are chosen, then up to 11 OpenMP threads can be employed to accelerate the solution. The product of the number of OMP threads and MPI ranks must equal the number of cores per node. This results in a setup on Onyx for 1280 cores allocated across 4 MPI ranks per node with 11 OMP threads distributed across a total of 320 nodes. Additionally, testing revealed that distributions consistent with the nonuniform memory access (NUMA) structure of a node provide better results so it is important to select the number of subdomains that will take advantage of this. Relating this back to Onyx and its 2x 22 core nodes, it is best if the OMP threads and MPI processes are 4x11, 2x22, 1x44, etc, however, not all combinations work with a certain number of ranks. Examples for 1280 ranks on Onyx and Narwhal are listed in Table 2.6. One can see the number of ranks is better aligned towards Narwhal as the available options for Onyx are only three. This could be changed if the grid points and grid partitioning are both adjusted to align with the 44 cores per node on Onyx. The computations in this thesis are carried out with 4 MPI processes and 11 OMP threads on Onyx and with 8 MPI processes and 16 OMP threads on Narwhal.

# 3. RESULTS

This chapter describes the results generated with the codes Kestrel, Wabash, and LASTRAC. It covers the heat transfer on the surface and a different streak formation occurring in low order solutions. It also discusses how the inlet condition is chosen for Wabash. Once the basic state is calculated, LASTRAC is used to conduct an LST study on the Kestrel and Wabash basic state. Several forcing schemes are used in DNS to investigate the effects and are defined along with the experiment and Hader's DNS cases in Table 3.1. The uniform forcing corresponds to Case U and involves a uniform distribution of forcing amplitude across frequencies. Quiet forcing corresponds to Case Q, and represent the spectrum of freestream fluctuations in the BAM6QT under quiet-flow operation, as shown in Figure 2.10. Noisy forcing corresponds to Case N, and represents the corresponding noisy-flow BAM6QT spectrum, as shown in Figure 2.10. With these forcing schemes, the heat transfer results and the spectra of locations in the boundary layer are analyzed. Finally, the results are compared to each other and with the experimental and computational results found by Chynoweth [2] and Hader [3], [19].

**Table 3.1**. DNS and experiment identification for plots.

| Chynoweth Run 1611 | Experiment |
|---|---|
| Uniform forcing | Case U |
| BAM6QT quiet flow | Case Q |
| BAM6QT noisy flow | Case N |
| Hader controlled forcing | Case HC |
| Hader random forcing | Case HR |

## 3.1 Low-order Calculations

Kestrel's main use in this project is to efficiently calculate an accurate laminar-flow result for the entire flared cone geometry. With an accurate laminar-flow solution, the inlet condition for direct numerical simulation with Wabash can be extracted. To check these results, Wabash and Kestrel were compared with each other on a common grid with similar order of accuracy settings. In order to do this, the nosetip must be removed and a numerically sharp nosetip is added. The mesh is described in a previous section and can be seen in Figure 2.5 and 2.7.

### 3.1.1 Numerically Sharp Nosetip Solution with Wabash and Kestrel

The numerically sharp laminar-flow solutions were computed in both Kestrel and Wabash. The skin friction coefficient magnitude can be seen in Figures 3.1 and 3.2. At first glance, the solutions look almost identical. However, adjusting the contours in Figure 3.3 and 3.4 illustrates the relatively small differences more clearly. In the figures, streaks can be seen at 90° degree intervals. Data along cirumferential lines on the cone surface were extracted to more clearly identify the magnitude and can be seen in Figure 3.5 and 3.6. These streaks are not large in magnitude, but could have a significant impact on the transition process. Computations were carried out to determine if the streaks were a numerical artifact related to grid smoothness and quality. Among other things, the subdomain locations were adjusted, overlapping for the periodic boundary conditions were adjusted, and half or quarter grids were used. In each case, the results were the same and showed periodic streaks. In the end, the hypothesis is that there are streaks inherent to the geometry and are stationary instabilities resulting from the curvature of the cone. Similar phenomena were observed in computations of HIFiRE-5b detailed by Porter et al. [41]. Although unexpected, the fact that both Kestrel and Wabash, employing different numerical methods, predict these steaks and give confidence in the results. Further similarities between Wabash and Kestrel results can be seen in a streamwise extract available in Figure 3.7.

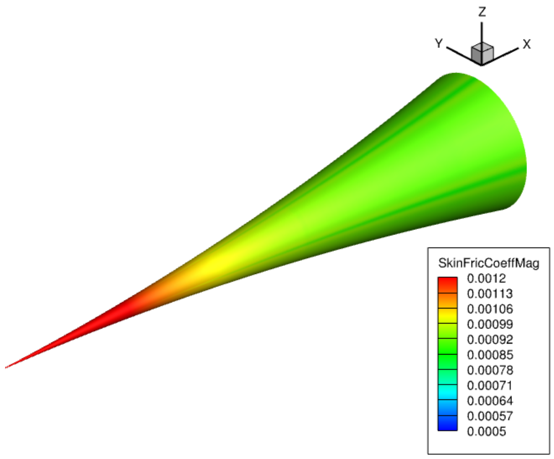


**Figure 3.1.** Kestrel: Numerically sharp solution displaying skin friction coefficient magnitude.

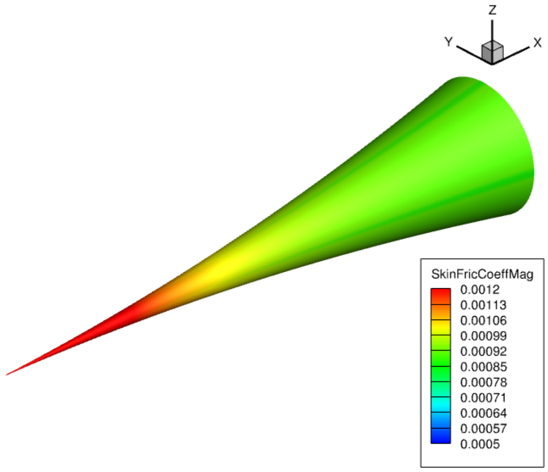


**Figure 3.2.** Wabash: Numerically sharp solution displaying skin friction coefficient magnitude.

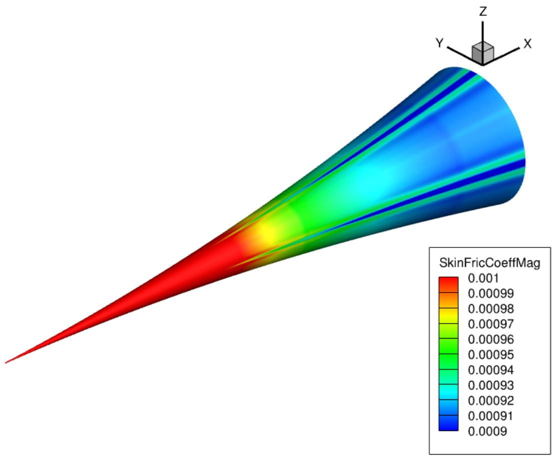


**Figure 3.3.** Kestrel: Numerically sharp solution with adjusted contours of skin friction coefficient magnitude.

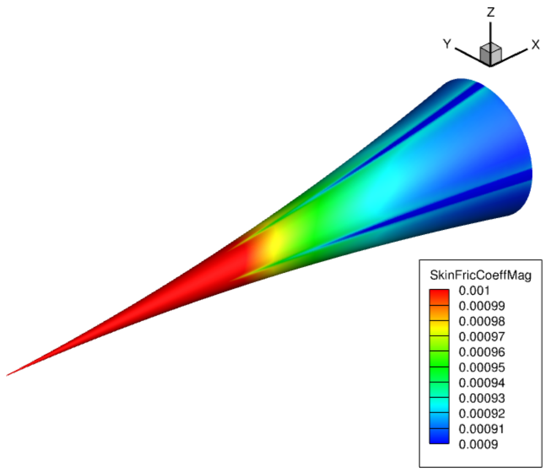


**Figure 3.4.** Wabash: Numerically sharp solution with adjusted contours of skin friction coefficient magnitude.

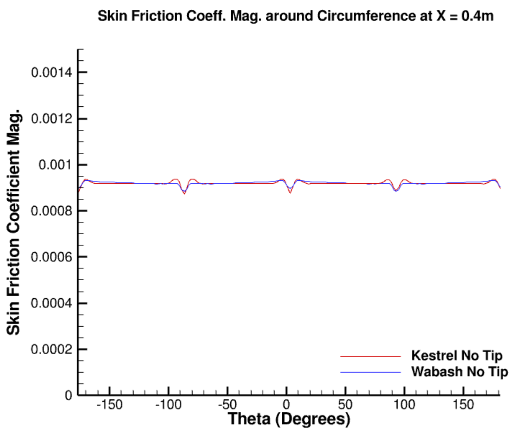


**Figure 3.5.** Circumferential skin friction coefficient magnitude at $x$ = 0.4m.

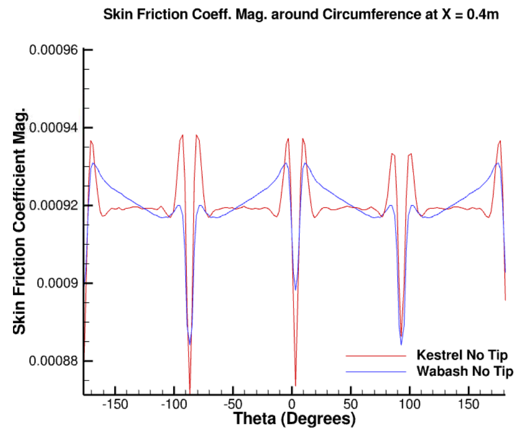


**Figure 3.6.** Adjusted circumferential skin friction coefficient magnitude at $x$ = 0.4m.

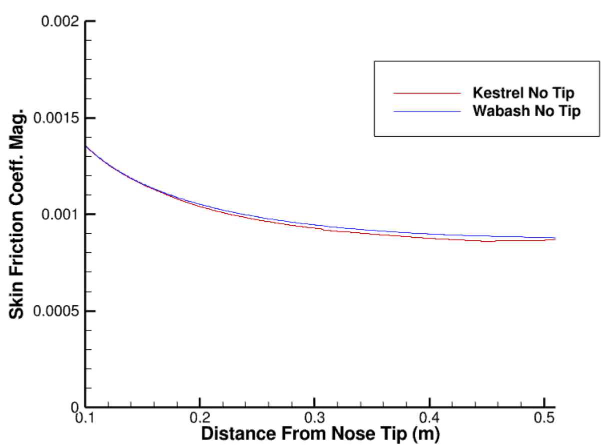


**Figure 3.7.** Streamwise skin friction coefficient magnitude taken down the center of a streak.

### 3.1.2 Modeled Nosetip Solution and Inflow Extraction

With Kestrel producing similar results to Wabash, a higher resolution mesh was created for the modeled nosetip to be the initial stage for DNS. Solution convergence is ensured by investigating the skin friction coefficient magnitude as the iterations continued. Figure 3.8 presents skin friction coefficient magnitude plotted for various iterations. It is focused on the location of extraction and all iterations fall within 1%. The skin friction coefficient contour is available in Figure 3.9 and 3.10. Additionally, comparisons between this and the numerically sharp tip are shown in Figure 3.11. Again, there are large streaks separated 90° apart. With higher resolution, smaller streaks are also visible and is similar to what Porter observed found as he increased grid resolution. With the basic state computed in Kestrel,

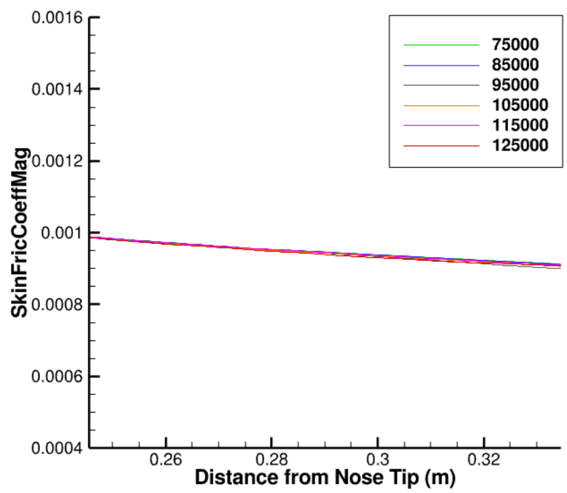


**Figure 3.8.** Skin friction coefficient magnitude by iteration count.

a profile can now be extracted to apply to the inlet of the DNS. The location is determined by the grid generation process of the DNS. The extraction is very carefully done as to match the start of the DNS grid perfectly. The location of the extraction can be seen in Figure 3.12. This data is treated as axisymmetric and interpolated on to the entire inlet plane of the DNS. The boundary condition for the DNS inlet is set so that these values do not change during the duration of the DNS.

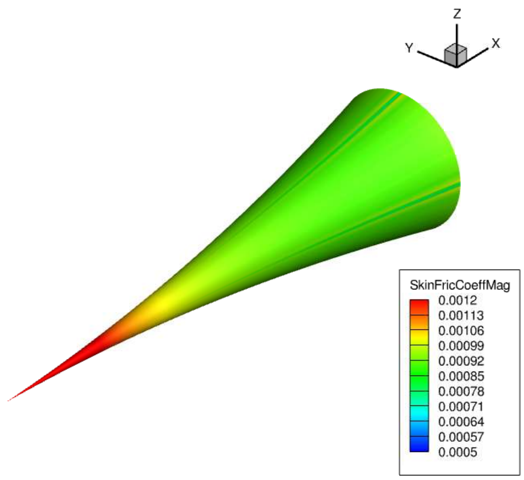


**Figure 3.9.** Kestrel: Modeled nosetip with skin friction coefficient magnitude contours.

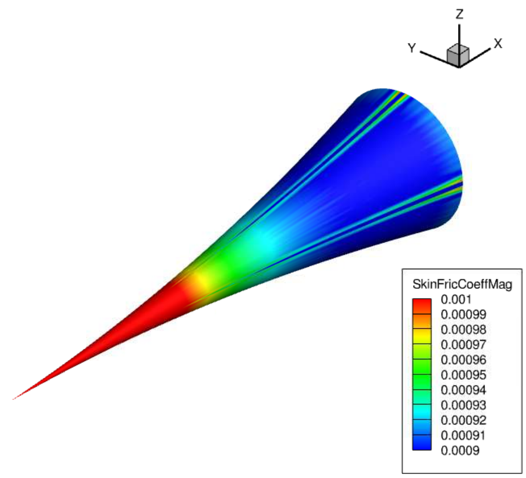


**Figure 3.10.** Kestrel: Modeled nosetip with adjusted skin friction coefficient magnitude contours.

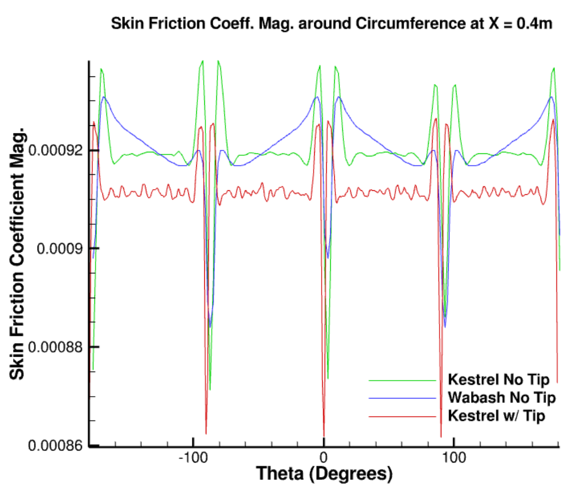


**Figure 3.11.** Skin friction coefficient magnitude comparison with Kestrel with no tip, Kestrel with a tip, and Wabash with no tip.

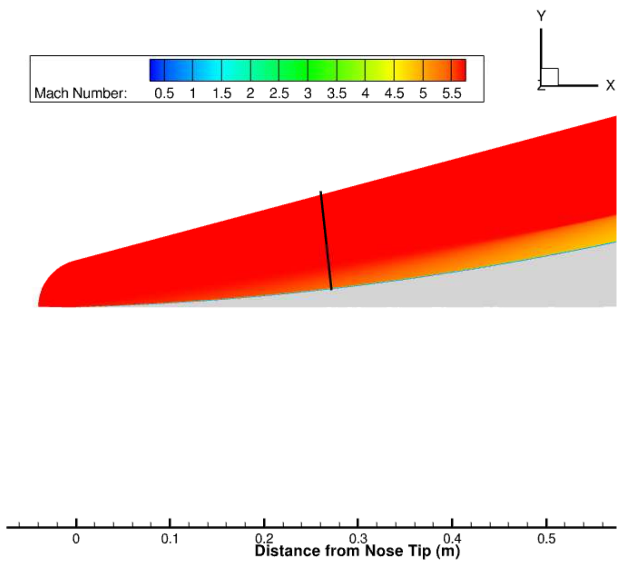


**Figure 3.12.** Location of DNS inflow extract.

### 3.2 DNS Basic State

The basic state of the DNS is computed with no forcing and a long run time. The rear of the cone can be seen in Figure 3.13. It is expected that the flow would be laminar the entire length, however, a small packet of rope waves can be seen. A close up of the density profile and density gradient magnitude can be seen in Figures 3.14 and 3.15. The cause of this may have to do with imperfections involving the inflow condition, the filter settings, numerical error such as truncation error and roundoff error, or from numerical noise introduced from the compact differencing scheme. However, it is reassuring that the flow develops the second mode instability on its own and that the addition of noise (forcing) leads to early transition. Additionally, the frequency for the second mode waves can be estimated using Equation 1.1. The boundary layer thickness is 1 mm and the edge velocity is 599 m/s. This results in an estimated frequency around 300 kHz. Along with surface and volume analysis, spectral analysis is conducted on all cases using wall pressure data. The statistics for these frequencies are collected at 0.375 m, 0.49 m, 0.55 m, and 0.58 m and are used to map the evolution of the unstable modes as they travel down the cone. The results for the basic state are in Figure 3.17 with Figure 3.16 as a reference to the locations. It is noted that the first location had an issue and can not be shown. However, each location after that shows a strong 300 kHz frequency with its harmonics gaining amplitude as they travel down the cone.

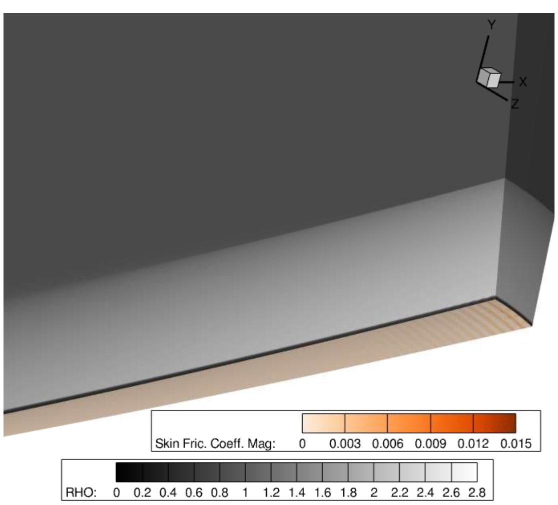


**Figure 3.13.** Basic state of the flared cone.

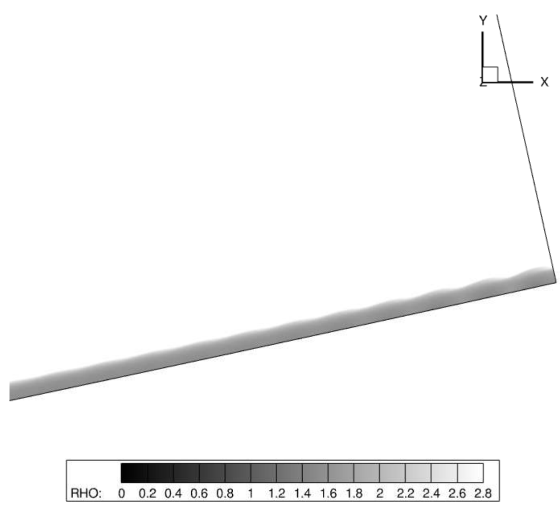


**Figure 3.14.** Density near the aft-body of the cone.

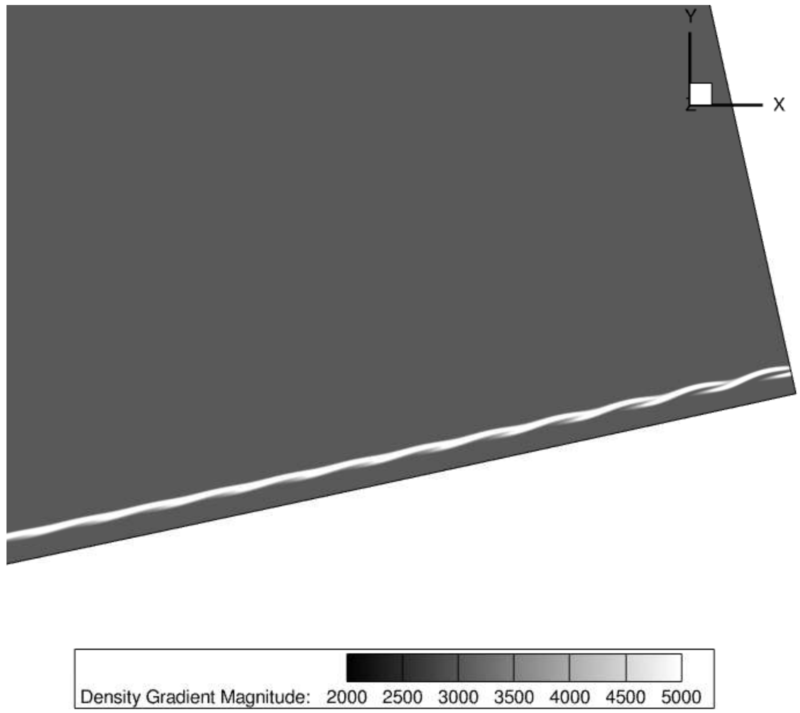


**Figure 3.15.** Density gradient magnitude detailing rope waves.

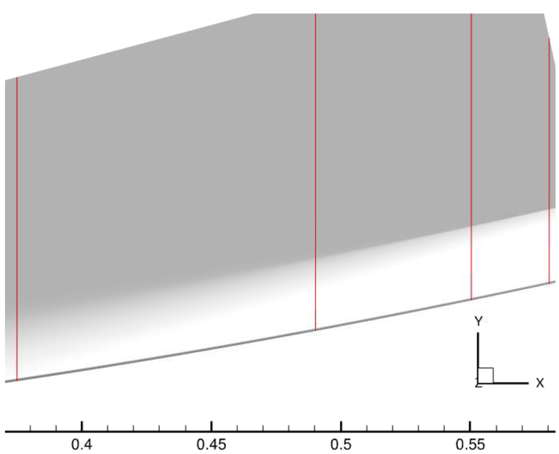


**Figure 3.16.** The four red lines correspond to the four locations where data is collected on the surface

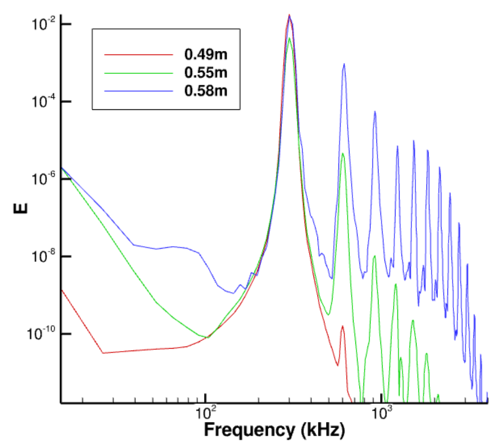


**Figure 3.17.** Energy for frequencies found at various $x$ locations on the surface of the cone

## 3.3 LASTRAC

Although there are signs of second-mode transition in the DNS basic state, it is important to confirm the unstable modes with a separate tool before more resources are spent on DNS with random forcing. A 2D slice is extracted from each basic state and used as inputs for LASTRAC. It then calculates the N-factors for selected frequencies at each station along the cone. The results calculated using the basic states obtained with Kestrel and Wabash can be seen in Figures 3.18 and 3.19. The most unstable modes are around 300 kHz, as seen in both figures. This result is close to the experimental findings for second mode instability and aligns with the estimation calculated above. The maximum N-factor for each mesh is different as the Wabash mesh does not have the same distance for the instabilities to grow. The black dotted line represents an N-factor of 12 and is drawn to compare the two cases. If the flow were to transition from the same frequency at an N-factor of 12, the Kestrel mesh would transition at a distance of around 0.35 m. In the DNS mesh, the transition is delayed to around 0.5 m for the same N-factor and frequency. Additionally, the N-factor vs frequency plot is available in Figure 3.20, and shows that the maximum amplitude is decreased compared to the Kestrel mesh. Again, this is from the shorter distance available for the disturbance to grow.

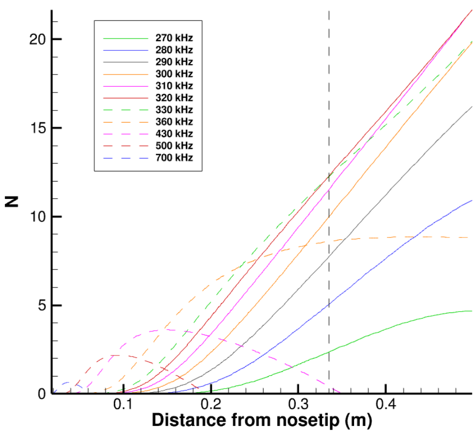


**Figure 3.18.** N-factors for frequencies along the Kestrel basic state. Black dotted line corresponds to N-factor equal to 12.

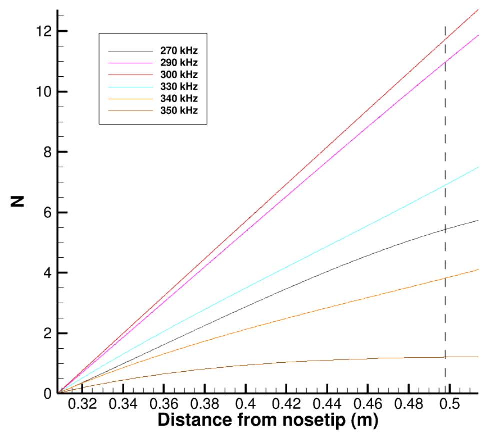


**Figure 3.19.** N-factors for frequencies along the Wabash basic state. Black dotted line corresponds to N-factor equal to 12.

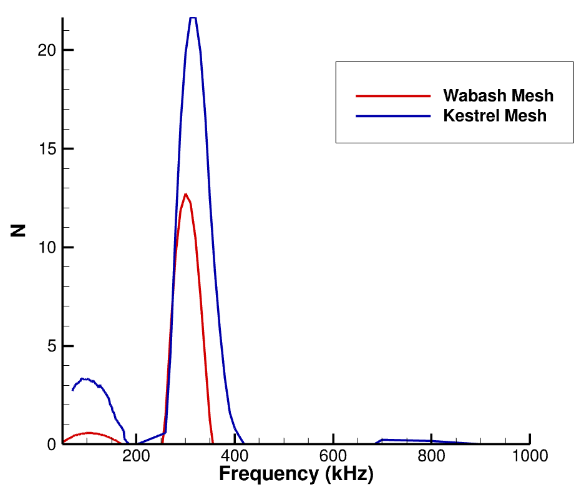


**Figure 3.20.** N-factor distribution for both Wabash and Kestrel basic state.

## 3.4 Random Forcing Outside of the Boundary Layer

There are a few ways to introduce the forcing and the initial thought is to introduce it outside of the boundary layer to allow it to naturally pass through the shock and enter the boundary layer as it does in wind tunnels or flight tests. The region of forcing is detailed as the box in Figure 3.21. This region is rotated around the $x$ axis to form a ring shape around the body. Various forcing strengths were used to find the value required to initiate

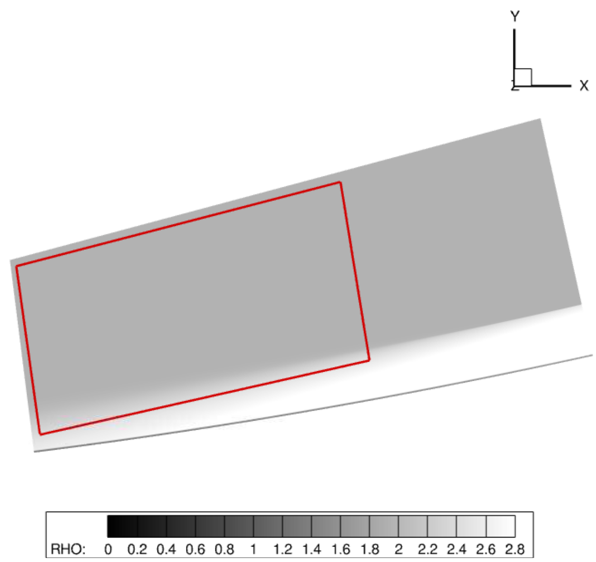


**Figure 3.21.** Location of forcing outside of boundary layer

transition. This involves using values of $A$ in Equation 2.8 as $1 \times 10^{-1}$, 1, 1.5, 3, 6, and 12. Unfortunately, this method was unsuccessful and resulted in no progress towards transition. The strongest forcing of 12 can be seen in Figure 3.22. There is a small packet of rope waves, but significant growth was not observed. Additionally, it is interesting to note that at a value of 12, the forcing is very large and can be seen disrupting the shock layer. In the end, further research is needed for the receptivity of disturbances into the boundary layer.

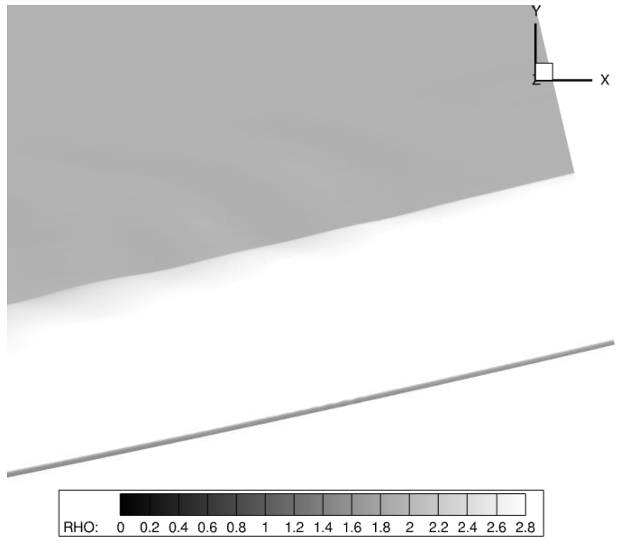


**Figure 3.22.** Very strong forcing visible with no significant effect on the boundary layer

### 3.5 Random Forcing within the Boundary Layer

With no success with the previous forcing scheme, the forcing is now placed in the boundary layer. It covers the entire domain that is behind $x$=0.39 m and can be seen in Figure 3.23. A range of amplitudes was again used to try to find transition. In this case, the strengths consist of $1 \times 10^{-2}$, $1 \times 10^{-1}$, and 1. This time, there is an effect and more notable transition occurred at a strength of $1 \times 10^{-2}$. The density profile can be seen in 3.24 and rope waves are clearly visible. However, the location of the start of transition is not at the distance from the nosetip that was observed experimentally. This means more space or more forcing is needed for the rope waves to develop and breakdown. The forcing at a strength of $1 \times 10^{-1}$ also provides promising results, but the location again does not match experiment. The strength of 1 provided full transition, however, it is still not in the measured location. Unfortunately, using a strength larger than 1 causes the solution to stop because the forcing creates negative temperatures and pressures. Therefore, the uniform noise profile, quiet profile, and noisy profile, described in Section 2.5.2, are each used with a forcing strength of 1 for Case U, Case Q, and Case N, respectively.

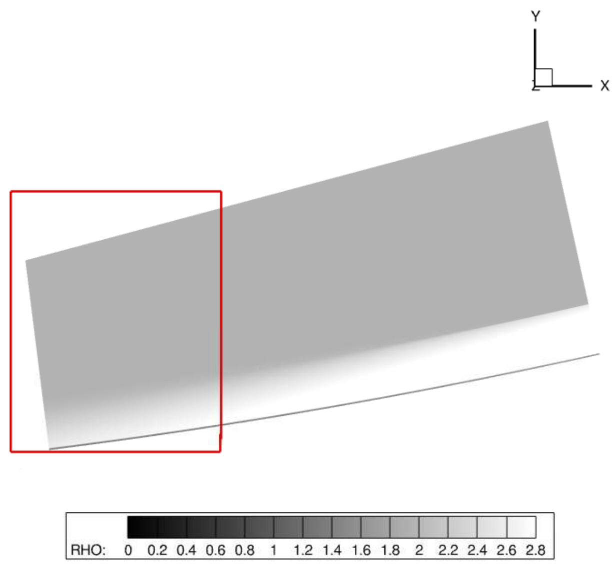


**Figure 3.23.** Forcing region with boundary layer included

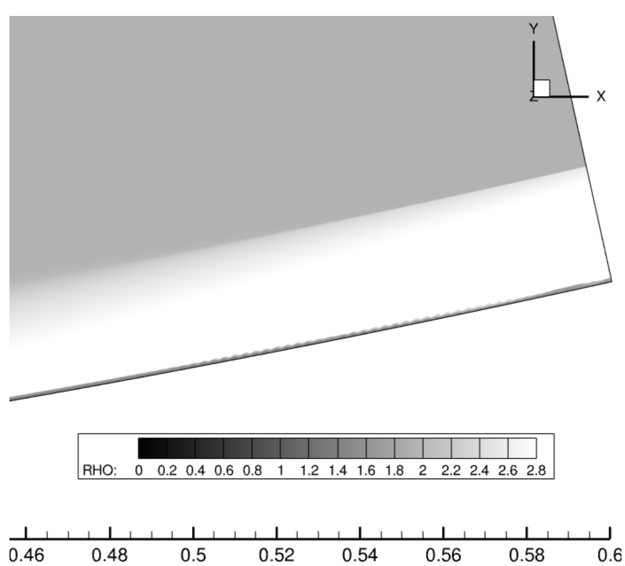


**Figure 3.24.** Start of transition with a strength of $1 \times 10^{-2}$

### 3.5.1 Case U

The uniform random forcing profile is able to cause the flow to transition and breakdown using a strength of 1. Figure 3.25 provides an overview of the region of interest showing instantaneous density and skin friction magnitude. In Figure 3.26, 2D axisymmetric waves can be seen and are similar to those observed near the end of the unforced solution. Figure 3.27, continues downstream and highlights secondary instabilities that form cross hatches as the 2D waves break down. Finally, Figure 3.28 shows a region of streamwise streaks forming before break down occurs in Figure 3.29. The time averaged heat transfer is available in Figure 3.30 and the primary and secondary streak formation that Chynoweth and Hader found can clearly be seen. To better visualize what is going on, Q-criterion is used to create iso-surfaces colored by streamwise vorticity. Figure 3.31a shows the axisymmetric waves and highlights a rise in heating to their deformation. Figure 3.31b details the secondary instabilities that create crossed vortices which contribute to high skin friction seen more clearly in Figure 3.32. Down stream of these features, streamwise vortices begin to form and create streaks on the surface. Eventually, these vortices gather energy through complex interactions and break down to form the secondary streak location as seen in Figure 3.31c. Additionally, spectral analysis is carried out using wall pressure data and Figure 3.33 shows the location of the analysis locations relative to the flow structure. The resulting frequency results are available in Figure 3.34. The first location at 0.375 m is still within the forcing region and reflects the uniform forcing profile. At the location within prevalent rope waves, the energy for 300 kHz and its harmonics grow while the other frequencies are damped. As these rope waves start to break down, the energy spreads out. Finally, once the flow breaks down to turbulence, there is a smooth broadband energy distribution with no particularly strong frequencies.

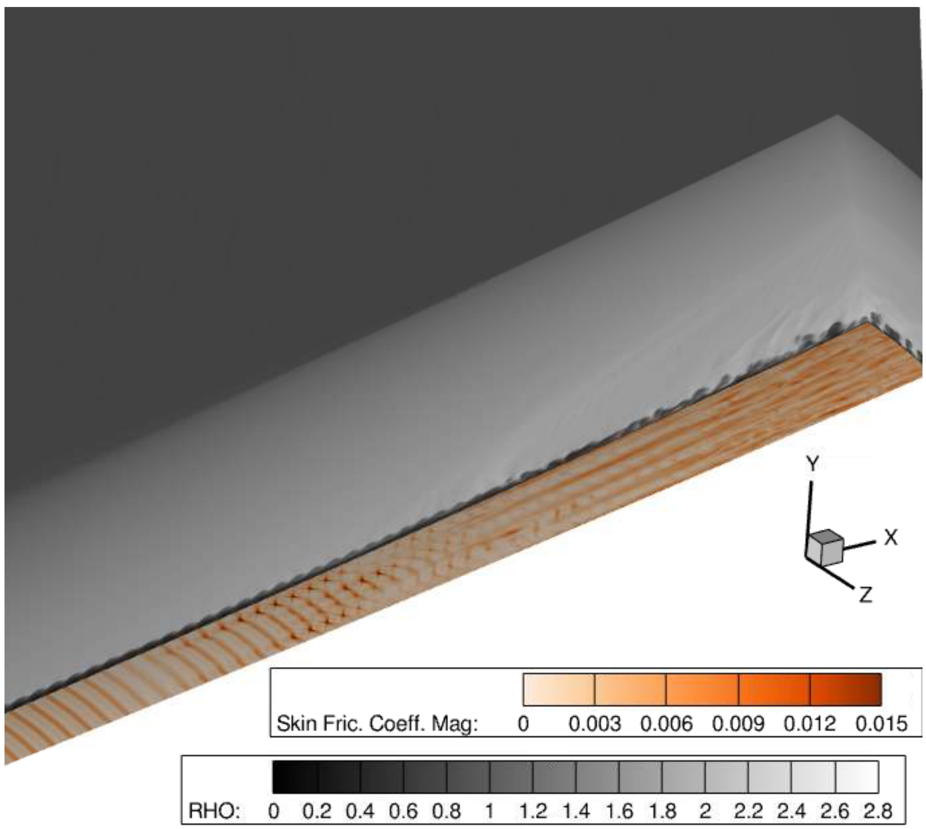


**Figure 3.25.** Case U: Transition to turbulence at a forcing strength of 1.

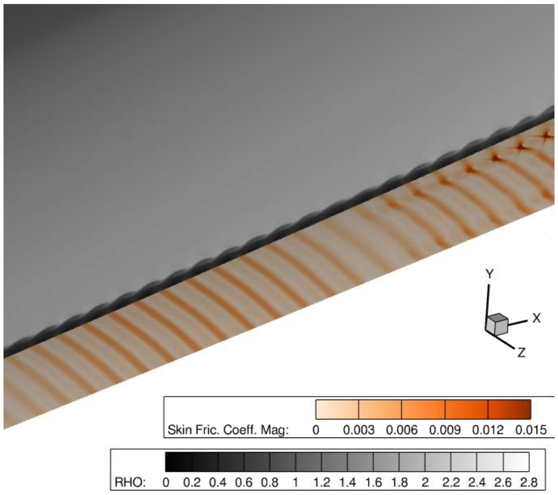


**Figure 3.26.** Case U: Axisymmetric waves with fluctuating magnitude.

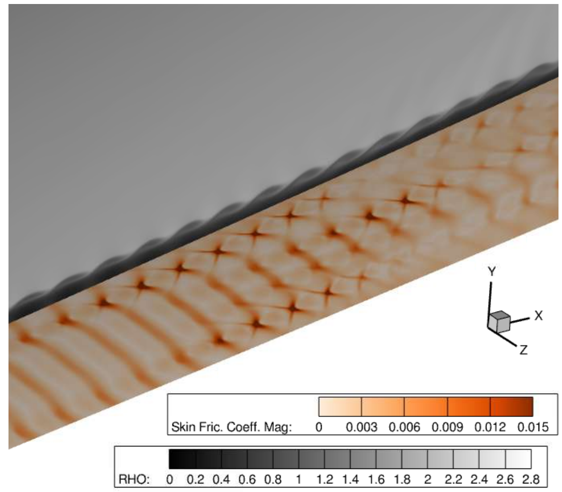


**Figure 3.27.** Case U: 2D waves break down and form cross hatches on the surface.

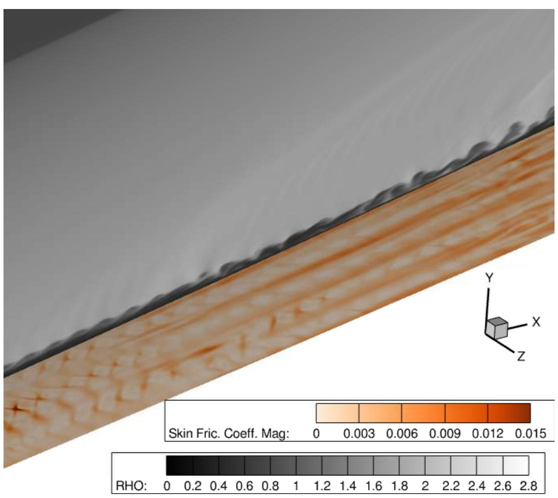


**Figure 3.28.** Case U: Vortices form which leave streaks on the surface.

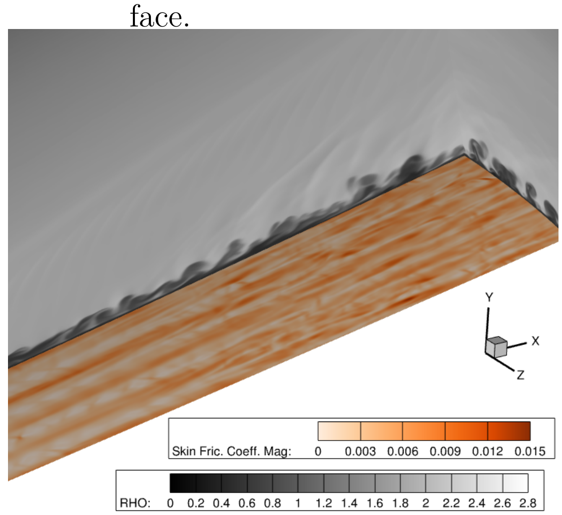


**Figure 3.29.** Case U: Vortices break down into turbulence.

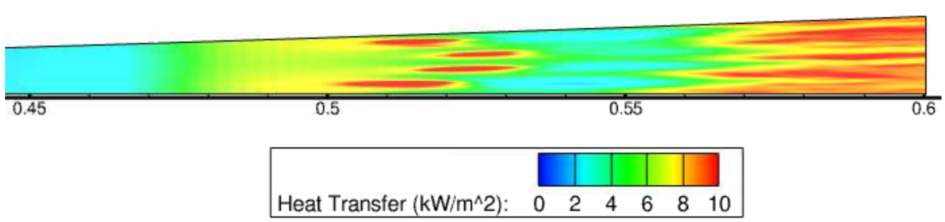


**Figure 3.30.** Case U: Time-averaged heat transfer on the surface of the cone.

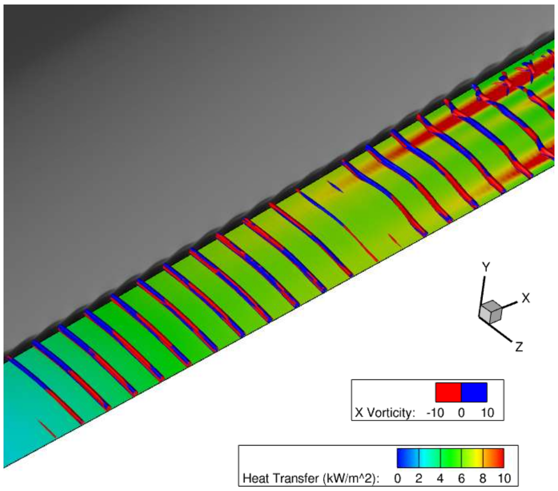


(a) Uniform heating until 2D waves start to deform.

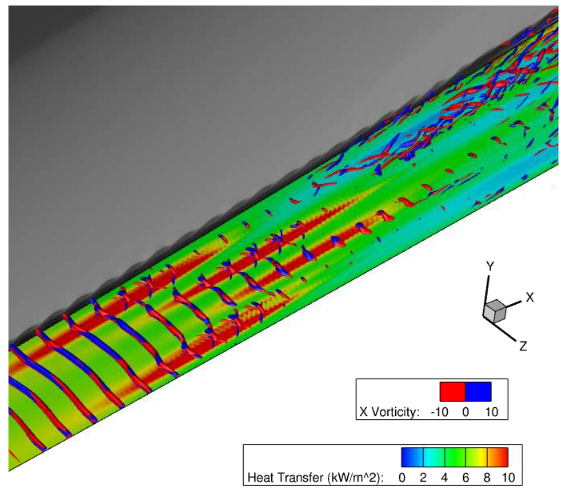


(b) Waves break down and cause intense heating.

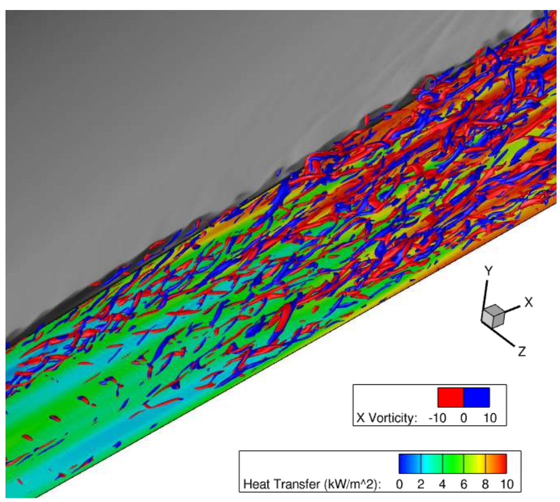


(c) Streamwise vortices form and increase in energy as they travel downstream.

**Figure 3.31.** Case U: Time-averaged heat transfer on the surface with Q-criterion iso-surface colored by $x$ vorticity. Density contour on the side.

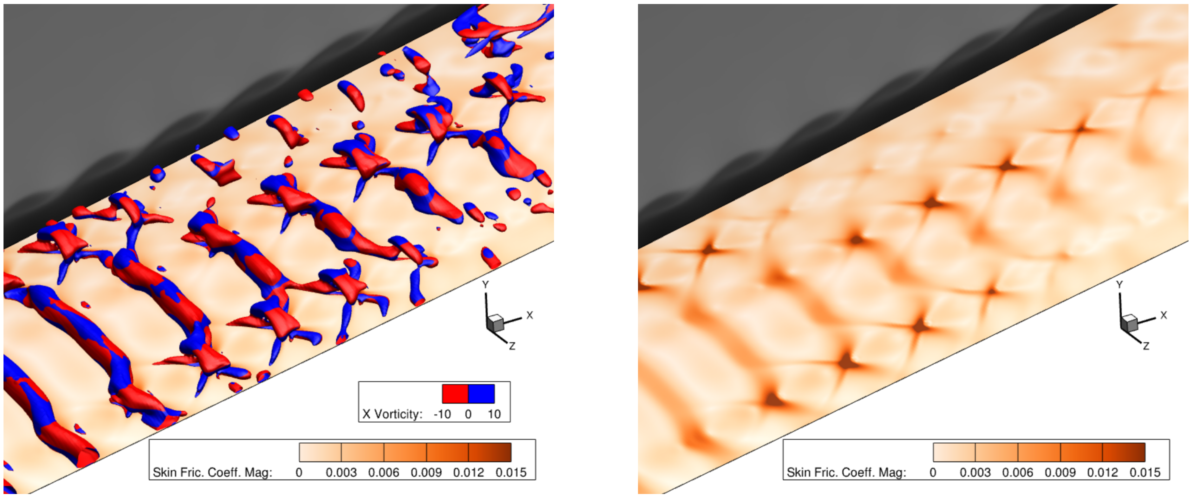


(a) Crossed vortices form as 2D waves break down.

(b) Crossed vortices contribute to high skin friction cross hatches.

**Figure 3.32.** Case U: Detailing the effect of the crossed vortices.

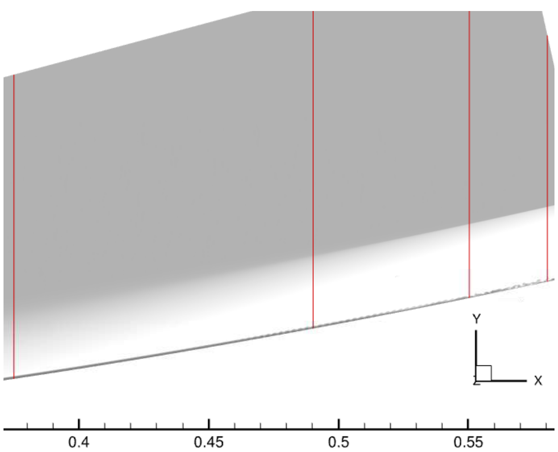


**Figure 3.33.** Case U: The red lines correspond to the locations where data is collected on the surface.

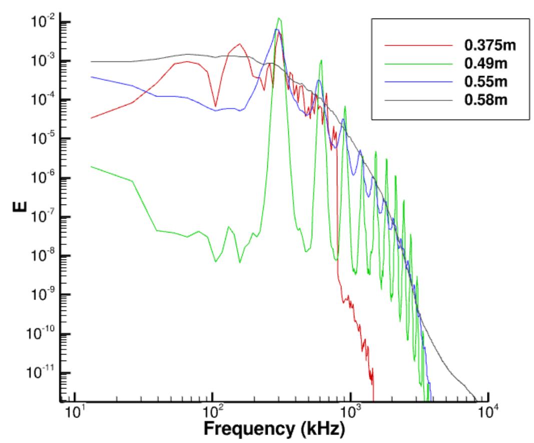


**Figure 3.34.** Case U: Energy for frequencies found at various $x$ surface locations.

### 3.5.2 Case Q

With successful results from uniform forcing, the profile of the quiet flow in the BAM6QT was applied next. In Figure 3.35, transition can be seen beginning on the cone, although it is later compared to the uniform forcing. The same mechanisms are occurring on with this setup and results in a time-averaged heat transfer contour seen in Figure 3.36. Additionally, the flow structure is shown with Q-criterion and vorticity in Figures 3.37b and 3.37a. The heating increases when the 2D waves break down and the flow evolves into streamwise vortices. These then cause the secondary set of streaks on the cone when they gain enough energy. In this case, secondary streaks do not have much space to develop because transition started later. In addition to these results, spectral analysis was carried out in the same way as before. Figures 3.38 and 3.39 show the location of the data relative to the flow structure and the energetic frequencies, respectively. The quiet forcing profile does not contain as many higher frequency signals compared to Case U, which is why the energetic frequencies drop so sharply at 100 kHz for the location of 0.375 m. However, the primary unstable mode at 300 kHz can already be seen to grow. As the disturbance moves downstream, the primary mode continues to grow in amplitude along with the harmonics also. Near the end of the cone, the flow is breaking down to turbulence and energy is being dispersed along the frequency band. It is noted that it does not fully break down. A more realistic comparison of the cases would involve calibrating forcing strength to the quiet flow forcing profile instead of the uniform forcing as it is done here. If the transition location for quiet flow can be shifted to the observed location by adjusting the forcing strength, then the other cases would have more realistic results if ran at that strength.

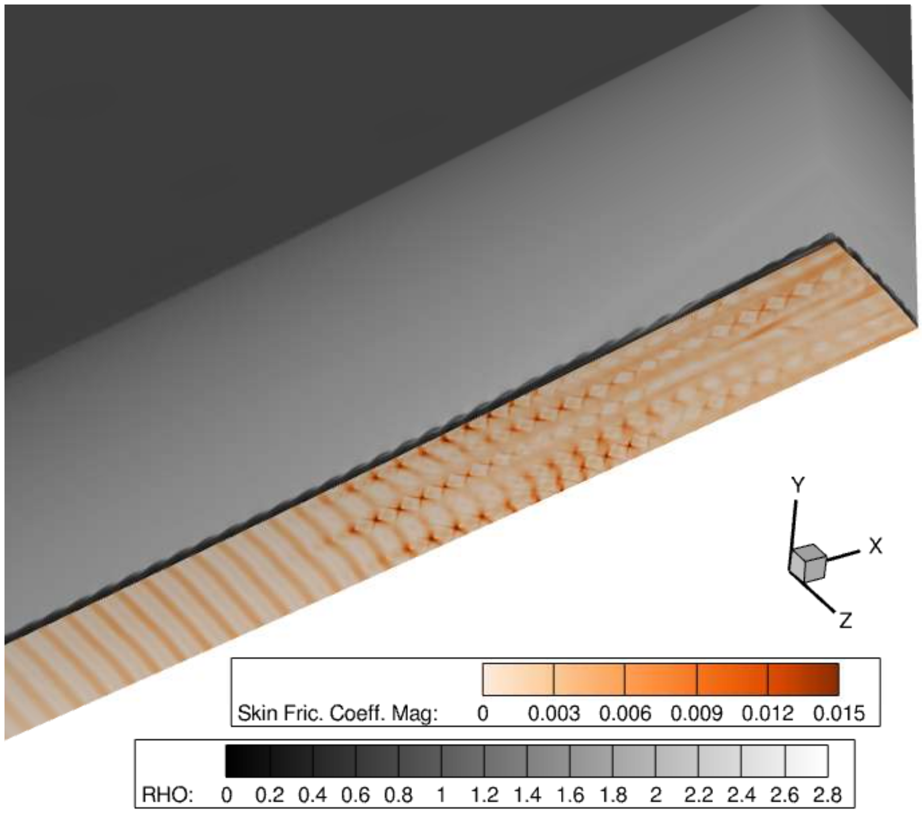


**Figure 3.35.** Case Q: Transition at a strength of 1.

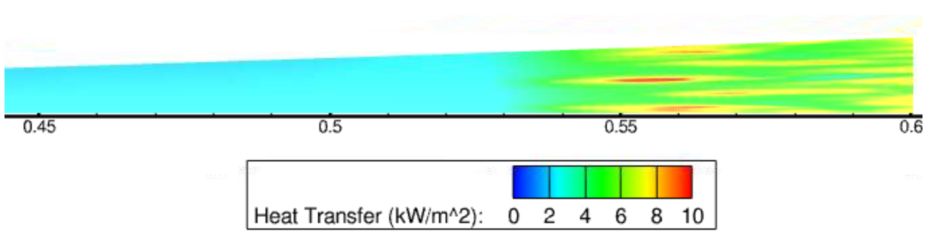


**Figure 3.36.** Case Q: Time-averaged heat transfer on the surface of the cone.

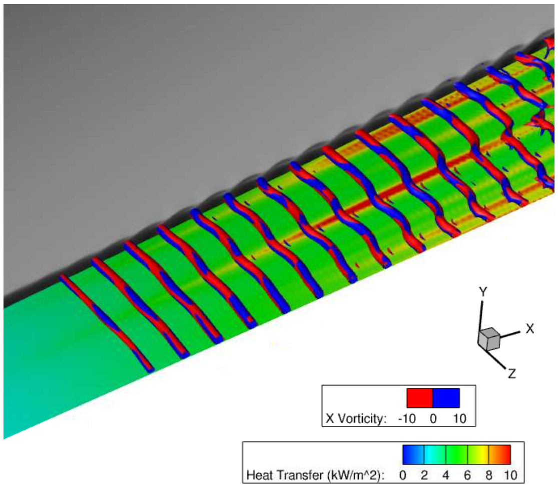


(a) Heating increases when 2D waves deform and breakdown.

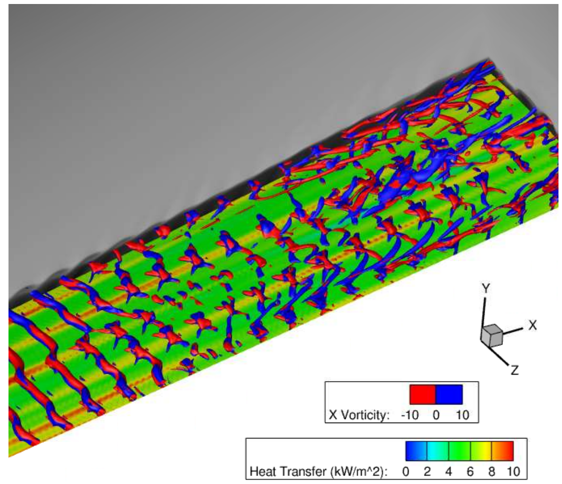


(b) Streamwise vortices form after 2D wave breakdown.

**Figure 3.37.** Case Q: Time-averaged heat transfer on the surface with Q-criterion iso-surface colored by $x$ vorticity. Density contour on the side.

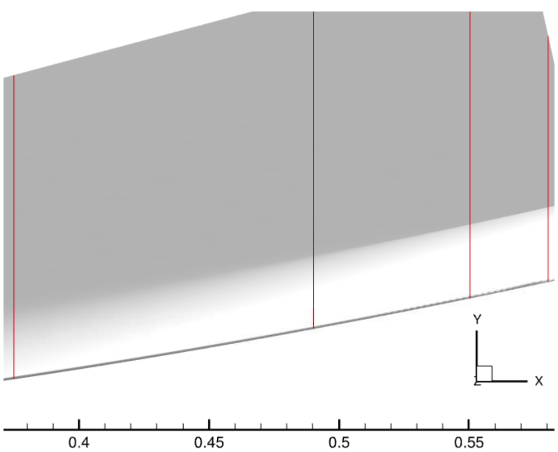


**Figure 3.38.** Case Q: The red lines correspond to the locations where data is collected on the surface.

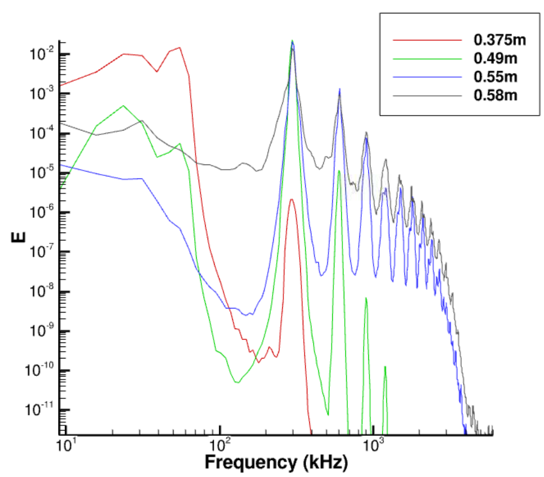


**Figure 3.39.** Case Q: Energy for frequencies found at various $x$ surface locations.

### 3.5.3 Case N

The last forcing scheme used is the noisy flow profile from the BAM6QT. In contrast to the quiet flow profile, it has a larger frequency range. This forcing scheme also achieved transition and can be seen in Figure 3.40. It has similar patterns as the previous cases, but it transitions more fully compared to Case Q. The heat transfer in Figure 3.41 has similar behavior compared to the uniform forcing, but transition begins further downstream. The flow structure can be seen in Figure 3.42 and follow the same pattern as before. The frequency analysis also showed similarities to the uniform case and can be seen in Figures 3.43 and 3.44. The first location is in the forcing region and reflect the random forcing profile. Similar to Case U and Q, the unstable modes and harmonics are amplified and then smooth out once the transitioning boundary layer evolves into turbulent flow. In this case, the boundary layer is breaking down to turbulence at the end, but it does not fully breakdown. The unstable mode and its harmonics can still be identified by their energy peaks.

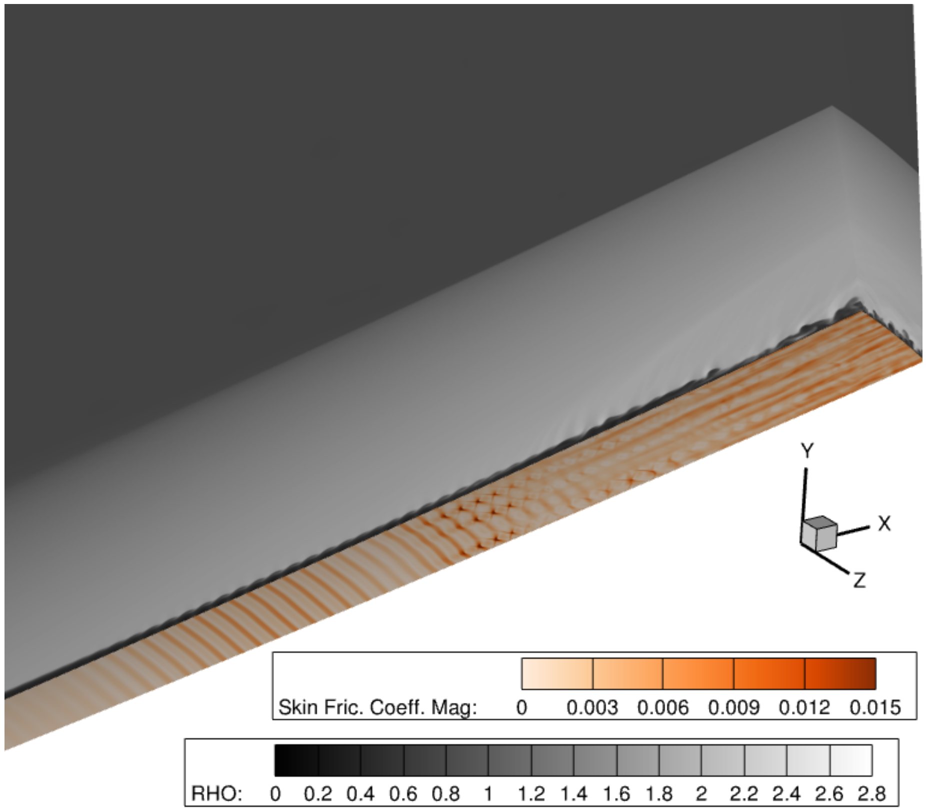


**Figure 3.40.** Case N: Transition at a strength of 1

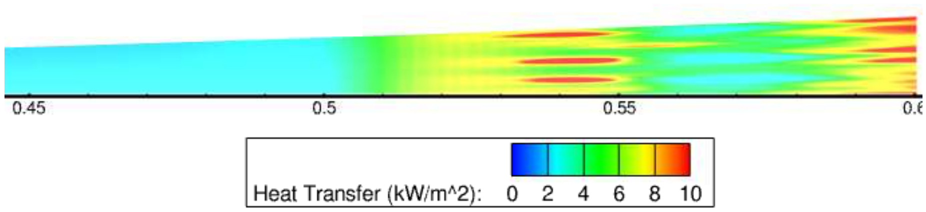


**Figure 3.41.** Case N: Time-averaged heat transfer on the surface of the cone.

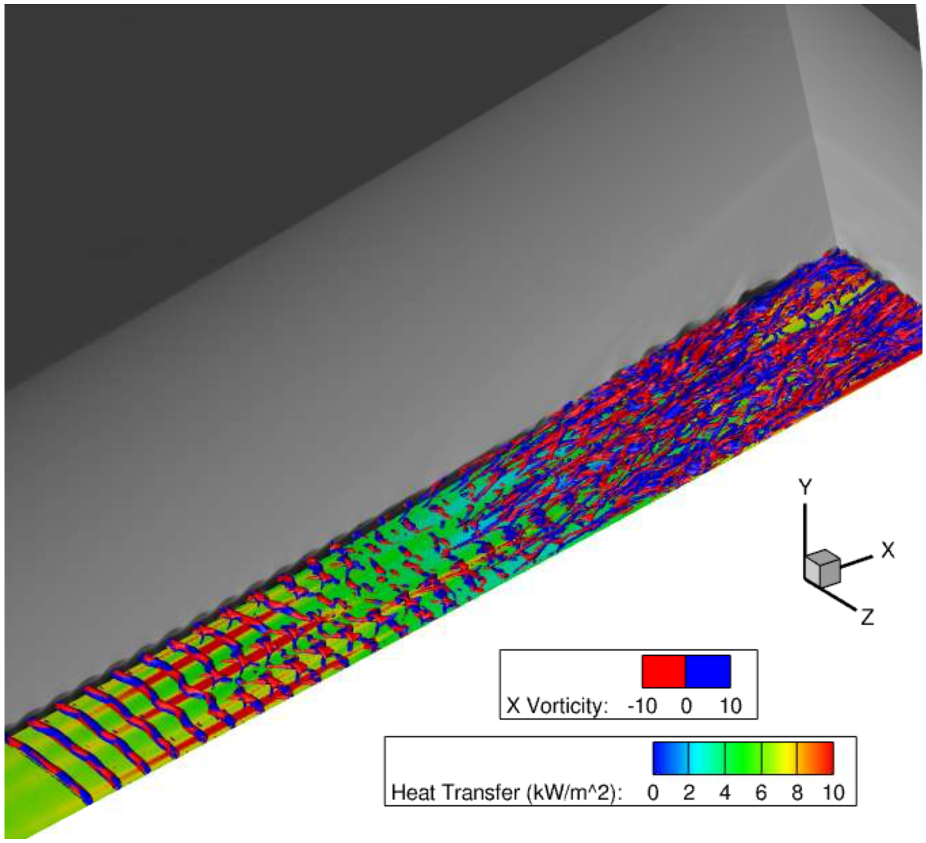


**Figure 3.42.** Case N: Q-criterion iso-surfaces with density contour on the side and time-averaged heat transfer on the bottom. This shows similar breakdown as Case U.

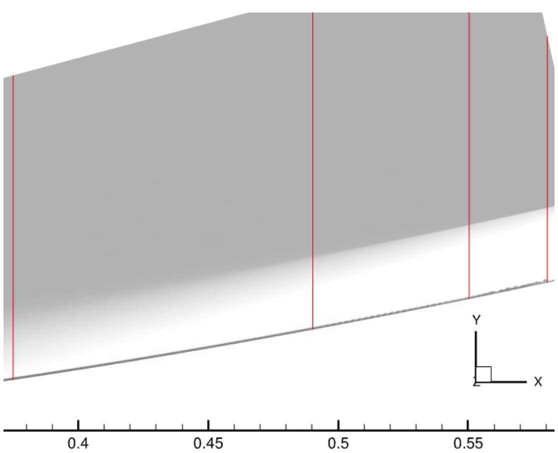


**Figure 3.43.** Case N: The red lines correspond to the locations where data is collected on the surface.

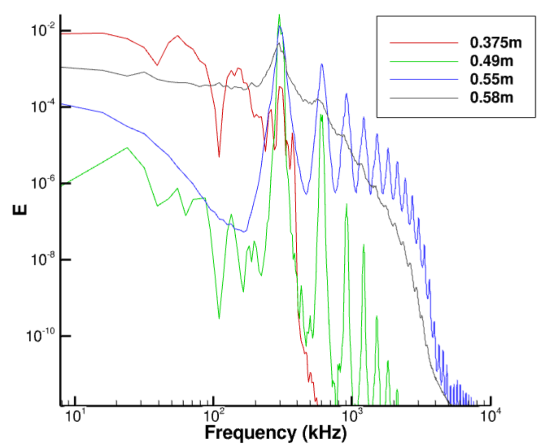


**Figure 3.44.** Case N: Energy for frequencies found at various $x$ surface locations.

### 3.5.4 Comparisons

With all of the cases completed, they are now compared with experimental heat transfer results from Chynoweth and computational results by Hader. Contours of heat transfer for each case can be seen in Figure 3.45. The computational results are axially extrapolated using periodicity to half of the cone circumference to better compare with the experiment. This is done because the DNS results only comprise of a 10° sector around the circumference. The basic state has an increase in heat transfer near the end of the cone where the rope waves are forming. This increase in heat transfer precedes the primary streak formation in Case U, Q, and N. With the slight disturbances introduced from the inlet and numerical scheme, the basic state cone could fully transition if given more space. It might be possible to remove these disturbances by adjusting the filter settings. After this slight increase in heat transfer, the primary streaks occur soon after and can be found in Case U, Case Q, and Case N. Following the primary streaks, there is a period of decreased heating and can be seen in all cases. After the decreased heating, the flow begins to breakdown and heating increases again. This process can be seen in Case U and Case N, while Case Q transitions too late to fully see it. In all cases, the location of transition differs from experiment, but, qualitatively, Case U looks most similar to the experiment. Case U shows the entire transition process, including breakdown to turbulence at the end of the cone just as the experiment does.

However, the differences, recorded streamwise down a hot streak, are clearly seen in Figure 3.46. The cases are converted to Stanton number as Case HC and HR are at slightly different conditions. A summary of the conditions can be found in Table 3.2. An adjusted plot is provided in Figure 3.47 to better visualize the similarities if transition occurred in the same location. In all cases, there is the characteristic rise, fall, and rise again of heat transfer that correspond to the primary streaks, the region between, and the secondary streaks. Interestingly, both Case U and Case N have an increase in streamwise heating before the strong peak. This behavior is also seen in Case HC and in Case HR. Additionally, the spanwise distribution of heat transfer across the middle of the primary set of streaks is available in Figure 3.48. The DNS data is replicated using periodicity for comparison to the experimental data. The location of the primary streaks differed for each case so each one has different $x$ locations for the spanwise data. With this, Case Q seems to be more similar quantitatively. Not only is the magnitude along a streak is more similar to the experiment, but also the spanwise wavenumber matches more closely with the experimental streaks. A better wavenumber comparison of Case Q and experiment can be seen in Figure 3.49. On the other hand, Case U and Case N both have a higher spanwise wavenumer compared to the experiment. This and the higher magnitude peak heating could be the result of higher frequency disturbances introduced by the forcing schemes. Case Q, only has forcing under 75 kHz and this results in a smoother increase to the peak and a closer alignment to spanwise heating. A summary of these comparisons are available in Table 3.3 with $\Delta_{t,2}$ being the distance between start of transition and the start of the secondary streaks.

Investigating the Q-criterion iso-surfaces is difficult for cases using random forcing as they do not cleanly amplify the unstable mode. In Case HC, Hader was able to find $\Lambda$ vortices that develop into hairpins as the flow transitions. This behavior is evidence for K-type transition. He found these structures by using the controlled forcing at around 300 kHz and can be seen in Figure 1.5. Results from Case U can be seen in Figure 3.50 and they show hairpins and other interesting features. However, it is much more disorganized compared to Hader's results, as would be expected given the nature of the forcing. The larger range of disturbances could interact with the unstable mode and hide, prevent, or skip the $\Lambda$ vortices.

The first and last location of frequency analysis are compared to show the difference between the beginning of the instability versus the breakdown for Case U, Q, and N. The first location is within the forcing region so it can show the difference between the initial input and the resulting effect. Figures 3.51 and 3.52 show the first location and last location for each case. The overall differences in forcing show that Case U and N are similar while Case Q has a much smaller frequency range. However, Case U does have some higher frequency disturbances than compared to Case N. The result of this difference is that case N does not transition fully while case U does. It is possible the energy in the higher frequencies contributed to Case U transitioning slightly earlier than Case N. Case Q has even lower energy with the lower range of forcing and as a result it transitions much later Case U and Case N. However, it still has significant amplitudes of the unstable mode and its harmonics.

As previously mentioned, an area of improvement is to match transition with experiment using the quiet forcing profile rather than attempting with uniform forcing. This could calibrate the random forcing profiles to the wind tunnel and help obtain results that more closely align with wind tunnel experiments.

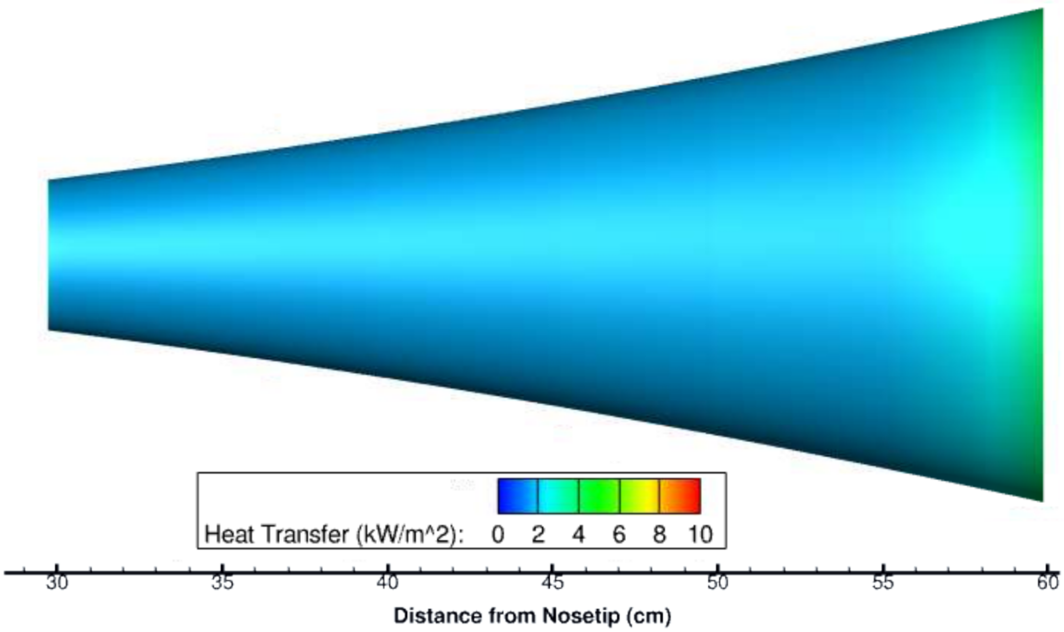


(a) Unforced Case

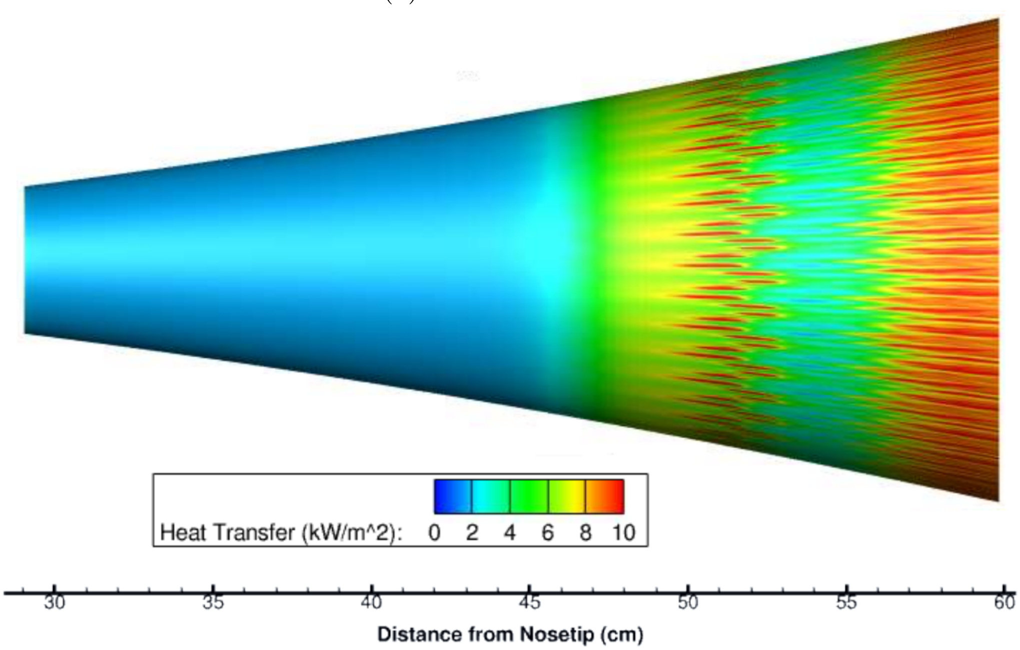


(b) Case U

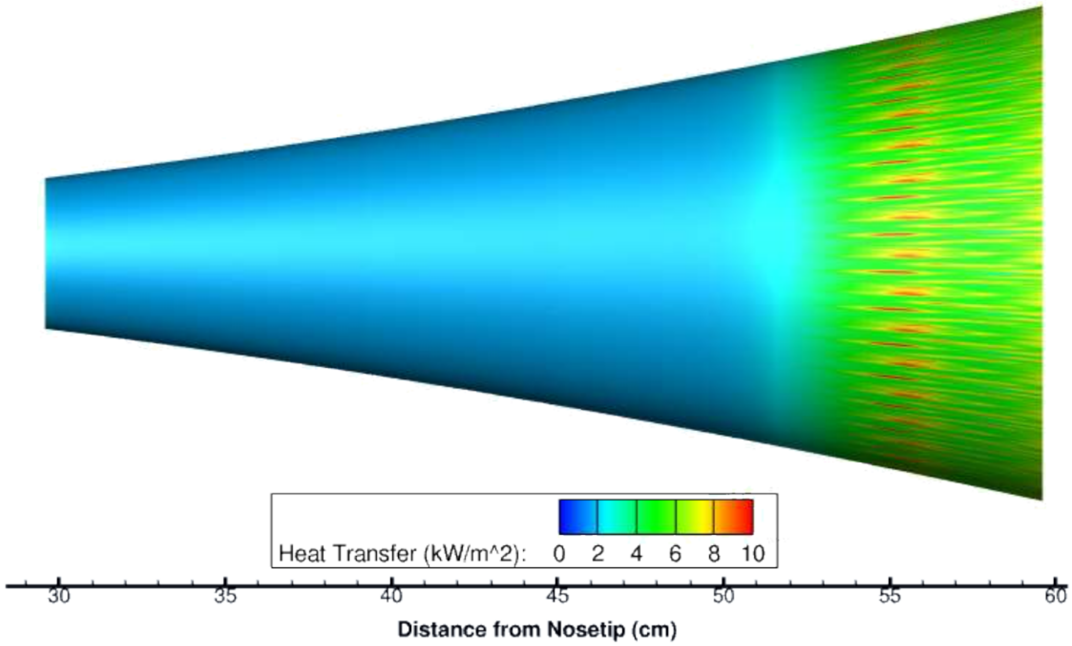


(c) Case Q

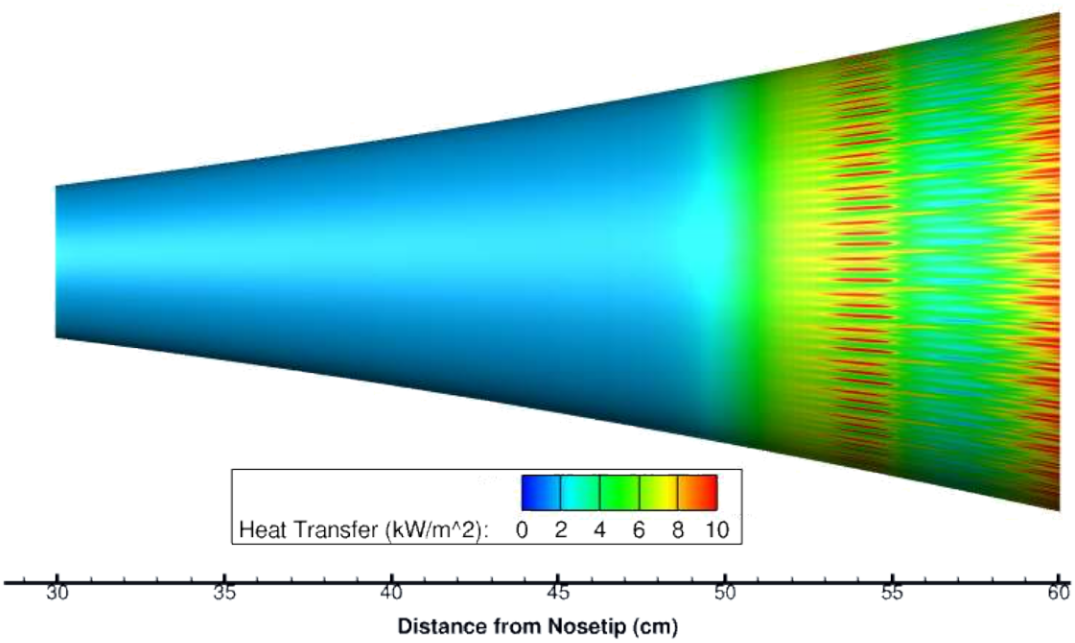


(d) Case N

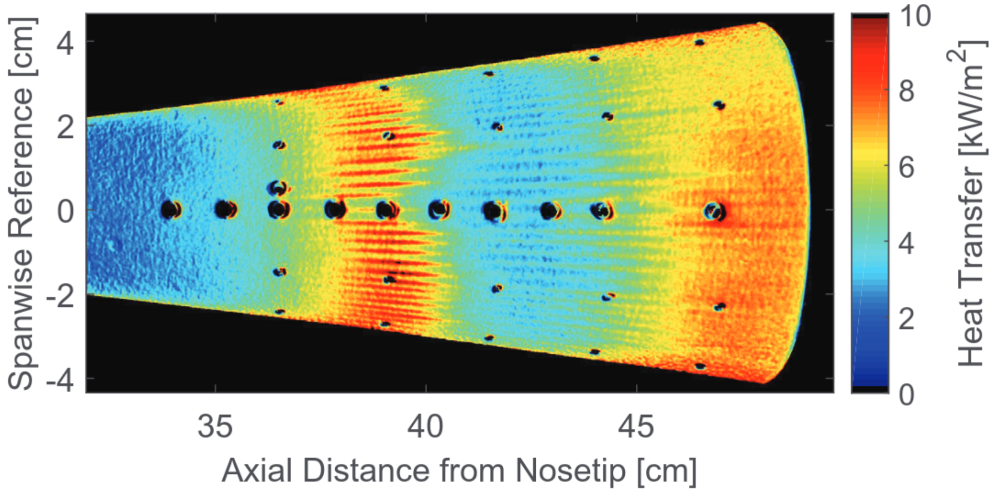


(e) Experiment [2]

**Figure 3.45.** Comparisons between heat transfer contours.

**Table 3.2**. Stagnation conditions for the experiment and DNS cases.

| | **Experiment** | **Case U, Q, N** | **Case HC, HR** |
|---|---|---|---|
| $Re$, 1/m | 12.1E6 | 12.1E6 | 10.8E6 |
| $T_0$, K | 422 | 422 | 420 |
| $P_0$, psi | 156.7 | 156.7 | 140 |

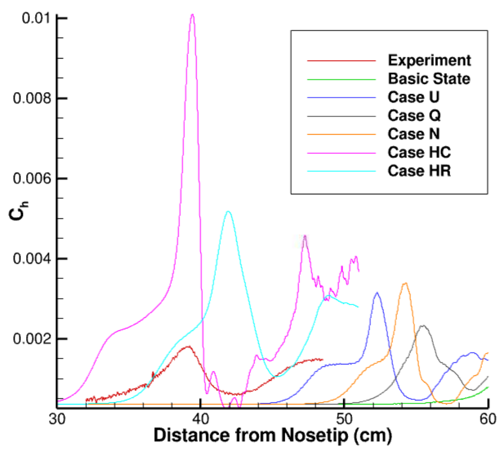


**Figure 3.46.** Stanton number streamwise along a primary streak. Experiment provided by [2]. Case HC and HR provided by [3].

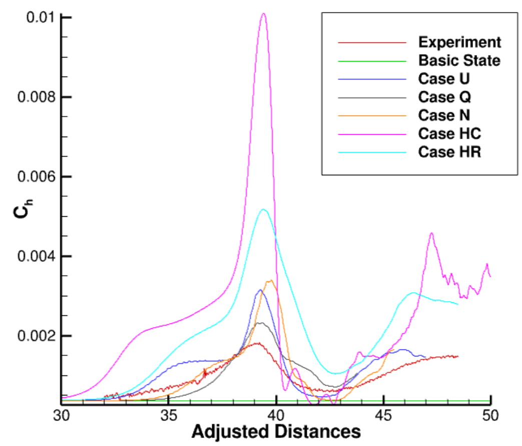


**Figure 3.47.** Locations of transition adjusted to compare with experiment.

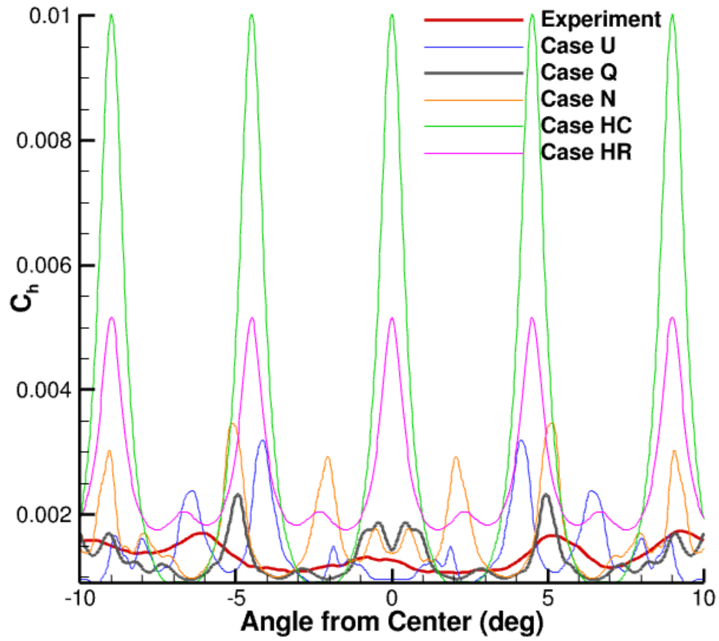


**Figure 3.48.** Spanwise data taken at the primary streak location. Experiment provided by [2]. Case HC and HR provided by [3].

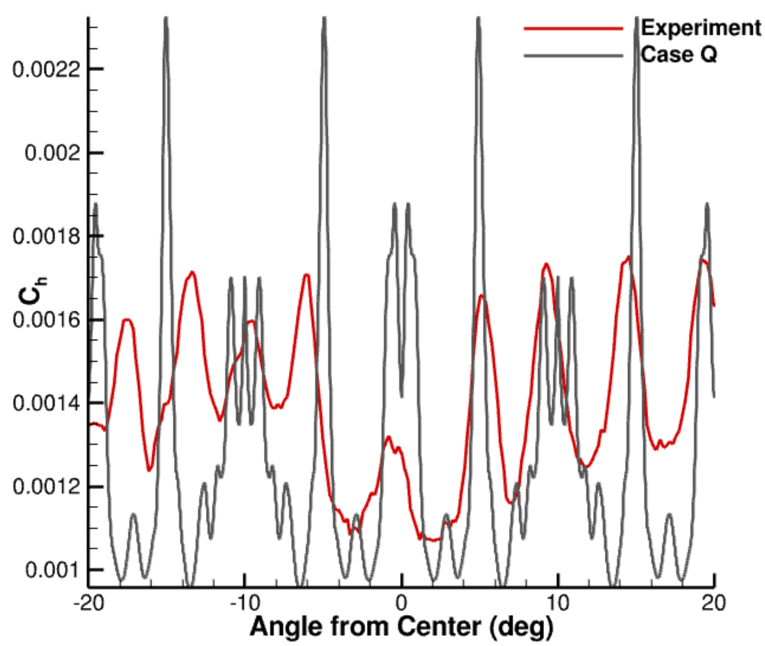


**Figure 3.49.** Case Q extended further to examine how well it matches with experiment.

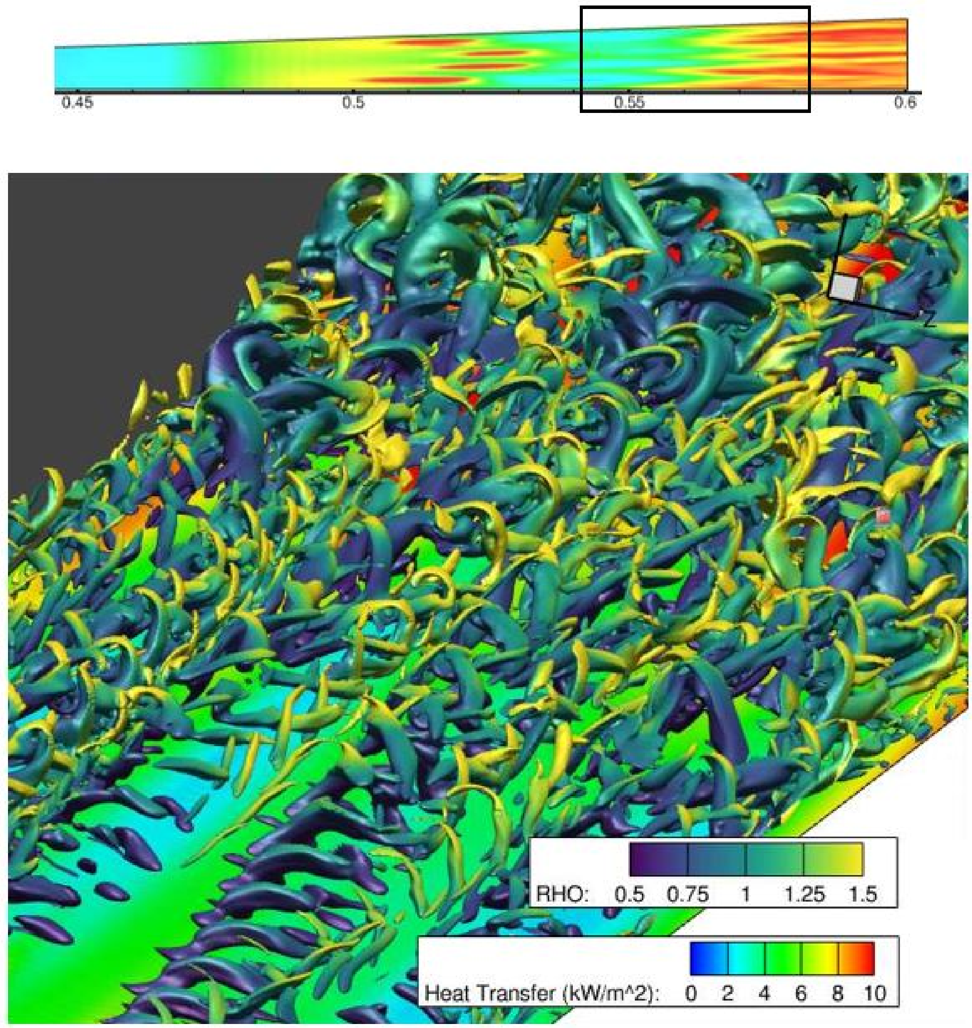


**Figure 3.50.** Case U: Close up of Q-criterion iso-surface colored by density with time-averaged heat transfer contour on the surface. The box in the heat transfer contour above indicates the viewing region.

**Table 3.3**. Summary of comparisons between the cases and experiment [2], [3].

| Case | Start of transition | Peak Heating ($C_h \cdot 10^3$) | Azimuthal Wavenumber | $\Delta_{t,2}$ |
|---|---|---|---|---|
| Experiment | 34 cm | 1.8 | 78 | 9.0 cm |
| Case U | 46 cm | 3.1 | 144 | 11 cm |
| Case Q | 52 cm | 2.3 | 81 | 8.0 cm |
| Case N | 50 cm | 3.4 | 126 | 8.0 cm |
| Case HC | 27.5 cm | 10 | 80 | 12 cm |
| Case HR | 33 cm | 5.1 | 80 | 10 cm |

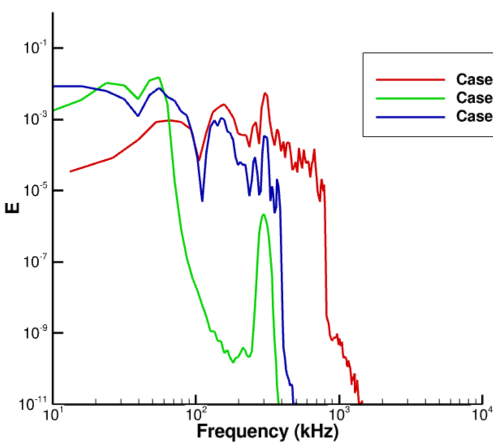


**Figure 3.51.** Spectra of cases at the beginning of the cone in the forcing region.

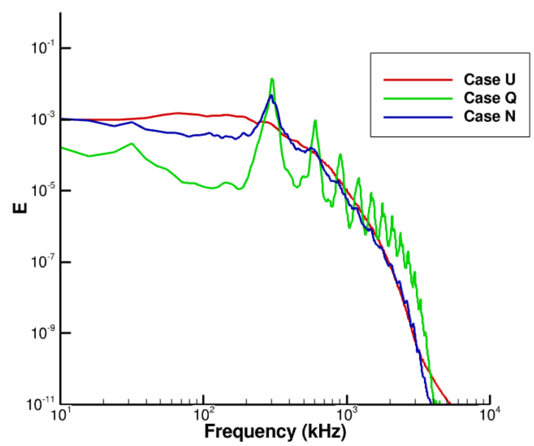


**Figure 3.52.** Spectra of cases at the end of the cone where the flow is breaking down.

# 4. CONCLUSION

Transition on a flared cone is achieved by conducting forced DNS using randomly generated traveling plane waves. The process starts with a lower order fully modeled solution and extracting a profile to use for the inlet of the DNS. During this stage, strong streamwise streaks are found at 90° locations around the cone. This is investigated by running multiple cases with two different solvers. In the end, these streaks are attributed to stationary instabilities caused by the geometry itself. Once the lower order calculation is done and the profile is extracted, a DNS basic state can be found on a cut off cone. Doing this allows a more cost efficient method to obtain DNS results on a sharp cone and avoids issues stemming from the nosetip. Once the basic state is calculated, LASTRAC, an LST solver, is used to verify the instabilities. LASTRAC successfully finds the unstable modes and is consistent with previous research done on the cone. LASTRAC identifies suspected issues on the DNS mesh for the growth of the unstable modes. The cut off cone for the DNS has significantly lower magnitude amplification and later amplification on the cone. Strong forcing is applied to compensate for this and the cone is extended 0.09 m to catch any transition that may occur too late. With this in mind, uniform forcing is applied with varying magnitudes to find and obtain transition. The strength is increased in an attempt to move transition to the correct location, however, the strength needed for this to occur led to numerical difficulties with the high-order code. The strongest force that could be applied is used for multiple random forcing schemes. These consist of uniform noise, the BAM6QT quiet flow profile, and the BAM6QT noisy flow profile. Each case achieves transition and qualitatively follows the behavior of the experimental results found by Chynoweth and the DNS results found by Hader. The transition location and the spanwise wavenumber generally did not match experiment. The discrepancies are likely due to the large amount of the cone that is cut off. Ideally, the cone cut off would be before any unstable modes start to amplify. According to LASTRAC results in Figure 3.18, this would be before 0.1m whereas the actual cut off is at 0.3m. The incorrect spanwise wavenumber could result from the interaction of higher frequency disturbances because the quiet flow profile, which has disturbances lower than 100 kHz, match with the experiment. The other two forcing profiles have disturbances that go as high as 700 kHz and result in higher spanwise wavenumbers. The Q-criterion is used to create visualizations of the flow structure. Hader was able to find $\Lambda$ vortices and track their evolution to hairpins using controlled forcing at the frequency of the unstable mode. With the random forcing used in this thesis, the flow is much more chaotic and interactions between the disturbances can hide or prevent the formation of the $\Lambda$ vortices. However, interesting flow structures can be seen along with hairpin vortices.

Overall, the DNS results are qualitatively accurate compared to Chynoweth's experimental results and Hader's computational results and using traveling plane waves as forcing was shown to work. The mechanisms for transition and breakdown are similar, but they occur at an a different location or with a different spanwise wavenumber. This discrepancy could be attributed to a few things, but most likely it is the result of cutting the cone at 0.3 m. It is recommended that further study capture more of the cone, preferably as close to 0.1 m as possible. This can be accomplished by implementing better overset capability or by using other methods to speed up the time step to allow the use of cell edge lengths smaller than $1 \times 10^{-5}$. In addition to this, it is recommended to calibrate the DNS using the quiet case. This can be done by adjusting the strength for the quiet case until transition occurs in the correct location. Once this is done, the other noise profiles should be tested at this strength. The results from Case Q provides evidence that this method of random forcing works and that implementing disturbance profiles from wind tunnel data may assist when trying to reproduce experiments. It is recommended to further research the using of forcing profiles related to wind tunnel noise.

# REFERENCES

[1] L. E. Steen, *Characterization and Development of Nozzles for a Hypersonic Quiet Tunnel*. Master's Thesis, Purdue University School of Aeronautics and Astronautics, ProQuest LLC, 2010.

[2] B. C. Chynoweth, *Measurements of Transition Dominated by the Second-Mode Instability at Mach 6*. Ph.D. Dissertation, Purdue University School of Aeronautics and Astronautics, ProQuest LLC, 2018.

[3] C. Hader, *Direct Numerical Simulations of Hypersonic Boundary-Layer Transition for a Flared Cone*. Ph.D. Dissertation, University of Arizona Department of Aerospace and Mechanical Engineering, ProQuest LLC, 2019.

[4] F. M. White, *Viscous Fluid Flow, Third Edition*. McGraw Hill, 2006.

[5] H. Schlichting and K. Gersten, *Boundary-Layer Theory, Ninth Edition*. Springer, 2017. DOI: 10.1007/978-3-662-52919-5.

[6] R. E. Mayle, "The Role of Laminar-Turbulent Transition in Gas Turbine Engines," Turbo Expo: Power for Land, Sea, and Air, vol. Volume 5: Manufacturing Materials and Metallurgy; Ceramics; Structures and Dynamics; Controls, Diagnostics and Instrumentation; Education; IGTI Scholar Award; General, Jun. 1991. DOI: 10.1115/91-GT-261.

[7] M. Gaster, "The structure and behavior of laminar separation bubbles," Cranfield University AERADE Reports Archive, Cranfield, UK, ARC R&M 3595, 1969.

[8] A. Fedorov, "Transition and stability of high-speed boundary layers," *Annual Review of Fluid Mechanics*, vol. 43, no. 1, pp. 79–95, 2011. DOI: 10.1146/annurev-fluid-122109-160750.

[9] W. S. Saric, H. L. Reed, and E. B. White, "Stability and transition of three-dimensional boundary layers," *Annual Review of Fluid Mechanics*, vol. 35, no. 1, pp. 413–440, 2003. DOI: 10.1146/annurev.fluid.35.101101.161045.

[10] F. Li and M. R. Malik, "Fundamental and subharmonic secondary instabilities of görtler vortices," *Journal of Fluid Mechanics*, vol. 297, pp. 77–100, 1995. DOI: 10.1017/S0022112095003016.

[11] N. Malmuth, A. Fedorov, V. Shalaev, *et al.*, "Problems in high speed flow prediction relevant to control," AIAA Paper 1998-2695. DOI: 10.2514/6.1998-2695.

[12] L. M. Mack, “Boundary-layer linear stability theory,” AGARD Report vol. 708, no. 3, 1984.

[13] J. L. Potter and J. D. Whitfield, “Boundary-layer transition under hypersonic conditions,” AGARDograph vol. 97, no.3, 1965.

[14] P. S. Klebanoff, K. D. Tidstrom, and L. M. Sargent, “The three-dimensional nature of boundary-layer instability,” *Journal of Fluid Mechanics*, vol. 12, no. 1, pp. 1–34, 1962. DOI: 10.1017/S0022112062000014.

[15] S. Bake, D. G. W. Meyer, and U. Rist, “Turbulence mechanism in klebanoff transition: A quantitative comparison of experiment and direct numerical simulation,” *Journal of Fluid Mechanics*, vol. 459, pp. 217–243, 2002. DOI: 10.1017/S0022112002007954.

[16] I. G. Currie, *Fundamental Mechanics of Fluids, Fourth Edition*. CRCC Press, 2013.

[17] E. Reshotko, “Boundary-layer stability and transition,” *Annual Review of Fluid Mechanics*, vol. 8, no. 1, pp. 311–349, 1976. DOI: 10.1146/annurev.fl.08.010176.001523.

[18] N. A. Jaffe, T. T. Okamura, and A. M. O. Smith, “Determination of spatial amplification factors and their application to predicting transition,” *AIAA Journal*, vol. 8, no. 2, pp. 301–308, 1970. DOI: 10.2514/3.5660.

[19] C. Hader and H. Fasel, “Towards simulating natural transition in hypersonic boundary layers via random inflow disturbances,” *Journal of Fluid Mechanics*, vol. 847, R3, 2018.

[20] W. Sutherland, “The viscosity of gases and molecular force,” *The London, Edinburgh, and Dublin Philosophical Magazine and Journal of Science*, vol. 36, no. 223, pp. 507–531, 1893. DOI: 10.1080/14786449308620508.

[21] F. G. Keyes, “A summary of viscosity and heat-conduction data for He, A, $H_2$, $O_2$, N, CO, $CO_2$, $H_2O$, and Air,” *Transactions of the American Society of Mechanical Engineers*, vol. 73, pp. 589–596, 1951.

[22] D. R. McDaniel, T. Tuckey, and S. A. Morton, “The HPCMP CREATE$^{TM}$-AV Kestrel Computational Environment and its Relation to NASA’s CFD Vision 2030,” AIAA Paper 2017-0813. DOI: 10.2514/6.2017-0813.

[23] D. R. McDaniel, “A Summary of New and Emergin Features in HPCMP CREATE$^{TM}$-AV Kestrel,” AIAA Paper 2021-0234. DOI: 10.2514/6.2021-0234.

[24] D. R. McDaniel and T. R. Tuckey, “HPCMP CREATE$^{TM}$-AV Kestrel New and Emerging Capabilities,” AIAA Paper 2020-1525. DOI: 10.2514/6.2020-1525.

[25] D. R. McDaniel and S. A. Morton, "HPCMP CREATE$^{TM}$-AV Kestrel Architecture, Capabilities, and Future Directions," AIAA Paper 2018-0025. DOI: 10.2514/6.2018-0025.

[26] J. Poggie, N. J. Bisek, and R. Gosse, "Resolution effects in compressible, turbulent boundary layer simulations," *Computers and Fluids*, vol. 120, pp. 57–69, 2015. DOI: 10.1016/j.compfluid.2015.07.015.

[27] K. M. Porter and J. Poggie, "Selective upstream influence on the unsteadiness of a separated turbulent compression ramp flow," *Physics of Fluids*, vol. 31, p. 016 104, 2019. DOI: 10.1063/1.5078938.

[28] J. Poggie and K. M. Porter, "Flow structure and unsteadiness in a highly confined shock-wave–boundary-layer interaction," *Physical Review Fluids*, vol. 4, p. 024 602, 2019. DOI: 10.1103/PhysRevFluids.4.024602.

[29] J. Poggie, N. J. Bisek, T. Leger, and R. Tang, "Implicit large-eddy simulation of a supersonic turbulent boundary later: Code comparison," AIAA Paper 2014-0423. DOI: 10.2514/6.2014-0423.

[30] M. W. Tufts, N. J. Bisek, and R. L. Kimmel, "Implicit large-eddy simulation of discrete roughness boundary-layer transition with added perturbations," AIAA Paper 2019-2967. DOI: 10.2514/6.2019-2967.

[31] A. Cerminara, A. Durant, T. André, N. Sandham, and N. J. Taylor, "DNS of acoustic receptivity and breakdown in a Mach 6 flow over a generic forebody," AIAA Paper 2018-0348. DOI: 10.2514/6.2018-0348.

[32] J. Poggie, *Forced DNS for Transition Prediction*. Unpublished, 2020.

[33] G. M. Andrews and J. Poggie, "Effects of freestream acoustic disturbances on hypersonic boundary layer stability," AIAA Paper 2020-2995. DOI: 10.2514/6.2020-2995.

[34] K. A. Gray, B. C. Chynoweth, J. B. Edelman, G. R. McKiernan, M. P. Wason, and S. Schneider, "Boundary-layer transition measurments in the Boeing/AFOSR Mach-6 Quiet Tunnel," AIAA Paper 2017-0068. DOI: 10.2514/6.2017-0068.

[35] A. J. Shuck, J. Poggie, and G. A. Blaisdell, "Preliminary computational study of transition on a flared cone using random forcing," AIAA Paper 2021-1204. DOI: 10.2514/6.2021-1204.

[36] L. Duan, M. M. Choudhari, A. Chou, *et al.*, "Characterization of freestream disturbances in conventional hypersonic wind tunnels," *Journal of Spacecraft and Rockets*, vol. 56, no. 2, pp. 357–368, 2019. DOI: 10.2514/1.A34290.

[37] C.-L. Chang, "The langley stability and transition analysis codes (LASTRAC) : LST, linear & nonlinear PSE for 2d, axisymmetric, and infinite swept wing boundary layers," AIAA Paper 2003-0974. DOI: 10.2514/6.2003-974.

[38] C.-L. Chang, "LASTRAC.3d: Transition prediction in 3d boundary layers," AIAA Paper 2004-2542. DOI: 10.2514/6.2004-2542.

[39] OpenSFS and EOFS. "About the lustre file system." (2021), [Online]. Available: https://www.lustre.org/about/.

[40] D. J. Garmann, *Characterization of the vortex formation and evolution about a revolving wing using high-fidelity simulation*. Ph.D. Dissertation, University of Cincinnati Department of Aerospace Engineering and Engineering Mechanics, OhioLINK, 2013.

[41] K. M. Porter, J. Poggie, and R. L. Kimmel, "Laminar and turbulent flow calculations for the HIFiRE-5b flight test," AIAA Paper 2017-3132. DOI: 10.2514/6.2017-3132.